







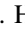







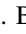

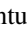

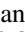




The KMOS^{3D} Survey: Investigating the Origin of the Elevated Electron Densities in Star-forming Galaxies at $1 \lesssim z \lesssim 3$

Rebecca L. Davies^{1,2,3} , N. M. Förster Schreiber¹, R. Genzel¹ , T. T. Shimizu¹ , R. I. Davies¹ , A. Schrubba¹, L. J. Tacconi¹ , H. Übler¹ , E. Wisnioski^{3,4} , S. Wuyts⁵ , M. Fossati⁶ , R. Herrera-Camus⁷, D. Lutz¹ , J. T. Mendel^{3,4} , T. Naab⁸ , S. H. Price¹ , A. Renzini⁹ , D. Wilman^{1,10} , A. Beifiori^{1,10} , S. Belli¹¹ , A. Burkert^{1,10} , J. Chan¹² , A. Contursi^{1,13}, M. Fabricius¹, M. M. Lee¹ , R. P. Saglia^{1,10} , and A. Sternberg^{14,15}

¹Max-Planck-Institut für extraterrestrische Physik, Giessenbachstrasse, D-85748 Garching, Germany; rdavies@swin.edu.au

²Centre for Astrophysics and Supercomputing, Swinburne University of Technology, Hawthorn, Victoria 3122, Australia

³ARC Centre of Excellence for All Sky Astrophysics in 3 Dimensions (ASTRO 3D), Australia

⁴Research School of Astronomy & Astrophysics, Australian National University, Canberra, ACT 2611, Australia

⁵Department of Physics, University of Bath, Claverton Down, Bath, BA2 7AY, UK

⁶Dipartimento di Fisica G. Occhialini, Università degli Studi di Milano-Bicocca, Piazza della Scienza 3, I-20126 Milano, Italy

⁷Departamento de Astronomía, Universidad de Concepción, Barrio Universitario, Concepción, Chile

⁸Max-Planck-Institut für Astrophysik, Karl-Schwarzschildstr. 1, D-85748 Garching, Germany

⁹INAF—Osservatorio Astronomico di Padova, Vicolo dell’Osservatorio 5, I-35122 Padova, Italy

¹⁰Universitäts-Sternwarte Ludwig-Maximilians-Universität München, Scheinerstr. 1, D-81679 München, Germany

¹¹Harvard-Smithsonian Center for Astrophysics, 60 Garden Street, Cambridge, MA 02138, USA

¹²Department of Physics and Astronomy, University of California, Riverside, CA 92521, USA

¹³IRAM, 300 Rue de la Piscine, F-38406 Saint Martin D’Hères, Grenoble, France

¹⁴School of Physics & Astronomy, Tel Aviv University, Ramat Aviv 69978, Israel

¹⁵Center for Computational Astrophysics, Flatiron Institute, 162 5th Avenue, New York, NY 10010, USA

Received 2020 August 7; revised 2020 December 15; accepted 2020 December 17; published 2021 March 8

Abstract

We investigate what drives the redshift evolution of the typical electron density (n_e) in star-forming galaxies, using a sample of 140 galaxies drawn primarily from KMOS^{3D} ($0.6 < z < 2.6$) and 471 galaxies from SAMI ($z < 0.113$). We select galaxies that do not show evidence of active galactic nucleus activity or outflows to constrain the average conditions within H II regions. Measurements of the [S II] λ 6716/[S II] λ 6731 ratio in four redshift bins indicate that the local n_e in the line-emitting material decreases from 187^{+140}_{-132} cm⁻³ at $z \sim 2.2$ to 32^{+4}_{-9} cm⁻³ at $z \sim 0$, consistent with previous results. We use the H α luminosity to estimate the rms n_e averaged over the volumes of star-forming disks at each redshift. The local and volume-averaged n_e evolve at similar rates, hinting that the volume filling factor of the line-emitting gas may be approximately constant across $0 \lesssim z \lesssim 2.6$. The KMOS^{3D} and SAMI galaxies follow a roughly monotonic trend between n_e and star formation rate, but the KMOS^{3D} galaxies have systematically higher n_e than the SAMI galaxies at a fixed offset from the star-forming main sequence, suggesting a link between the n_e evolution and the evolving main sequence normalization. We quantitatively test potential drivers of the density evolution and find that $n_e(\text{rms}) \simeq n_{\text{H}_2}$, suggesting that the elevated n_e in high- z H II regions could plausibly be the direct result of higher densities in the parent molecular clouds. There is also tentative evidence that n_e could be influenced by the balance between stellar feedback, which drives the expansion of H II regions, and the ambient pressure, which resists their expansion.

Unified Astronomy Thesaurus concepts: Galaxy evolution (594); High-redshift galaxies (734); Interstellar medium (847)

1. Introduction

The average properties of star-forming galaxies (SFGs) have evolved significantly from the peak epoch of star formation to the present-day universe. The cosmic star formation rate (SFR) density and the normalization of the star-forming main sequence (MS) have both decreased by an order of magnitude since $z \sim 2$ (e.g., Daddi et al. 2007; Elbaz et al. 2007; Madau & Dickinson 2014; Sobral et al. 2014; Speagle et al. 2014; Whitaker et al. 2014), primarily driven by the declining rate of cosmological cold gas accretion and the subsequent reduction in the molecular gas fractions of galaxies (e.g., Genzel et al. 2015; Scoville et al. 2017; Liu et al. 2019; Millard et al. 2020; Tacconi et al. 2020). The high gas fractions at $z \sim 2$ drive galaxy-wide gravitational instabilities, resulting in elevated gas velocity dispersions (e.g., Genzel et al. 2006, 2008; Law et al. 2009; Newman et al. 2013; Wisnioski et al. 2015;

Johnson et al. 2018; Krumholz et al. 2018; Übler et al. 2019) and triggering the formation of massive star-forming clumps (e.g., Elmegreen & Elmegreen 2005; Bournaud et al. 2007; Dekel et al. 2009; Genzel et al. 2011; Genel et al. 2012; Wisnioski et al. 2012; Wuyts et al. 2012c).

It is then perhaps not surprising that we also observe significant evolution of the properties of the interstellar medium (ISM). The first near-infrared spectroscopic surveys of high-redshift SFGs revealed that they do not lie along the locus of local SFGs on the [N II]/H α versus [O III]/H β diagnostic diagram, but are offset to higher line ratios (e.g., Shapley et al. 2005; Erb et al. 2006; Kriek et al. 2007). The physical origin of this offset remains highly debated, with proposed explanations including a harder ionizing radiation field (e.g., Steidel et al. 2016; Strom et al. 2017, 2018; Sanders et al. 2020), higher N/O abundance ratio (e.g., Masters et al. 2014, 2016; Jones et al. 2015; Shapley et al. 2015), elevated electron density

and ISM pressure (e.g., Dopita et al. 2016; D’Agostino et al. 2019), higher ionization parameter (e.g., Kashino et al. 2017; Bian et al. 2020), an increased contribution from shocks and/or active galactic nuclei (AGNs; e.g., Newman et al. 2014; Freeman et al. 2019), and/or a decreased contribution from diffuse ionized gas within the regions sampled by the observations (e.g., Shapley et al. 2019). It is very difficult to distinguish between different possible drivers based on the [N II]/H α and [O III]/H β ratios alone (e.g., Kewley et al. 2013), and it is necessary to quantify the evolution of each property to build a full picture of how the physical conditions in star-forming regions have evolved over time.

The electron density is typically measured using density-sensitive line ratios such as [S II] λ 6716/[S II] λ 6731, [O II] λ 3729/[O II] λ 3726, and C III] λ 1906/C III] λ 1909 (e.g., Osterbrock & Ferland 2006; Kewley et al. 2019). [S II] and [O II] have lower critical densities and ionization energies than C III], and therefore, these tracers probe the gas conditions in different regions of the ionized nebulae (e.g., Acharyya et al. 2019; Kewley et al. 2019). In this work, we focus on n_e measurements made using the [S II] and [O II] doublet ratios.

Emission-line studies of strongly lensed galaxies at $z \sim 1.5$ –3 provided the first hints that high- z SFGs have significantly larger electron densities than local H II regions (e.g., Hainline et al. 2009; Bian et al. 2010; Rigby et al. 2011; Christensen et al. 2012; Wuyts et al. 2012a, 2012b; Bayliss et al. 2014). Subsequent spectroscopic surveys found that the typical n_e in SFGs has decreased from $n_e \sim 200$ –300 cm^{-3} at $z \sim 2$ –3 (e.g., Steidel et al. 2014; Shimakawa et al. 2015; Sanders et al. 2016) to $n_e \sim 100$ –200 cm^{-3} at $z \sim 1.5$ (e.g., Liu et al. 2008; Kaasinen et al. 2017; Kashino et al. 2017) and to $n_e \sim 30$ cm^{-3} at $z \sim 0$ (e.g., Herrera-Camus et al. 2016; Kashino & Inoue 2019). However, the physical mechanism(s) responsible for driving this evolution are difficult to identify, and to date, no quantitative models have been proposed to explain the density evolution.

When interpreting n_e measurements, it is important to consider the geometry of the line-emitting material and the volume over which n_e is measured. Consider a H II region containing a collection of line-emitting structures with electron densities $n_{e,i}$, volumes V_i , and [S II] luminosities $L_{[\text{S II}],i}$. The [S II] λ 6716/[S II] λ 6731 ratio probes the approximate line-flux-weighted average n_e of these structures;¹⁶ i.e.,

$$n_e([\text{S II}]) \simeq \frac{\sum_i (n_{e,i} \times L_{[\text{S II}],i})}{\sum_i L_{[\text{S II}],i}} \quad (1)$$

The rms number of electrons per unit volume in the H II region, also known as the rms electron density or $n_e(\text{rms})$, can be calculated from the H α luminosity and volume of the H II region:

$$L(\text{H}\alpha, \text{H II}) = \gamma_{\text{H}\alpha} V_{\text{H II}} n_e^2(\text{rms}), \quad (2)$$

where $\gamma_{\text{H}\alpha}$ is the volume emissivity of H α (3.56×10^{-25} $\text{erg cm}^3 \text{s}^{-1}$ for Case B recombination at 10^4 K). The total H α luminosity of this hypothetical H II region can also be written as the sum of the H α luminosities of

the individual line-emitting structures:

$$L(\text{H}\alpha, \text{H II}) = \gamma_{\text{H}\alpha} \sum_i (V_i n_{e,i}^2). \quad (3)$$

By combining Equations (2) and (3), we can derive an expression for the volume filling factor (ff) of these structures:

$$ff \equiv \left(\sum_i V_i \right) / V_{\text{H II}} = n_e^2(\text{rms}) \times \frac{\sum_i V_i}{\sum_i (n_{e,i}^2 \times V_i)}. \quad (4)$$

Assuming that all of the line-emitting structures have roughly similar electron densities, and that the volume-weighted and light-weighted average densities are approximately equal, Equation (4) can be rewritten as

$$ff \simeq [n_e(\text{rms})/n_e([\text{S II}])]^2. \quad (5)$$

Observations of local H II regions have found that $n_e([\text{S II}])$ and $n_e([\text{O II}])$ are much larger than $n_e(\text{rms})$, implying that the majority of the line emission originates from clumps with relatively low volume filling fractions of $\sim 0.1\%$ –10% (e.g., Osterbrock & Flather 1959; Kennicutt 1984; Elmegreen & Hunter 2000; Hunt & Hirashita 2009; Cedrés et al. 2013). It is therefore likely that the physical processes governing the ionized gas densities occur on spatial scales far below what can be resolved at high z . However, global trends between n_e and galaxy properties provide constraints on what types of physical processes are most likely to drive the evolution of the global, line-flux-weighted average n_e in SFGs over cosmic time.

The electron density appears to be closely linked to the level of star formation in galaxies. Kaasinen et al. (2017) found that there is no difference in the electron densities of galaxies at $z \sim 0$ and $z \sim 1.5$ when they are matched in SFR. The electron density has been found to correlate with specific SFR (sSFR) and SFR surface density (Σ_{SFR}), at both low and high redshift (e.g., Shimakawa et al. 2015; Bian et al. 2016; Puglisi et al. 2017; Jiang et al. 2019; Kashino & Inoue 2019). There is also evidence for a spatial correlation between enhanced star formation activity and enhanced electron density in local galaxies (e.g., Westmoquette et al. 2011, 2013; McLeod et al. 2015; Herrera-Camus et al. 2016; Kakkad et al. 2018).

Several scenarios have been proposed to explain the correlation between n_e and the level of star formation. The initial n_e is set by the density of the parent molecular cloud, which also determines Σ_{SFR} through the Kennicutt–Schmidt relation. The radiation emitted by a star cluster dissociates and photoionizes the surrounding molecular gas to produce a H II region with a local electron density of $n_e \simeq 2 n_{\text{H}_2}$ (e.g., Hunt & Hirashita 2009; Shimakawa et al. 2015; Kashino & Inoue 2019). However, n_e may change over time as a result of energy injection and/or H II region expansion. The ambient density and pressure could significantly influence the dynamical evolution of H II regions. Oey & Clarke (1997, 1998) proposed that H II regions undergo energy-conserving expansion powered by stellar winds and supernovae (see also Weaver et al. 1977) until the internal pressure is on the order of the ambient pressure. H II regions in denser environments may expand less, resulting in larger electron densities (e.g., Shirazi et al. 2014; Herrera-Camus et al. 2016). Another possibility is that Σ_{SFR} , which sets the rate of energy injection by stellar winds and supernovae (e.g., Ostriker & Shetty 2011; Kim et al. 2013), may also govern the pressure and density in H II regions

¹⁶ This is true if the majority of the $n_{e,i}$ values fall in the regime where the relationship between n_e and [S II] λ 6716/[S II] λ 6731 is approximately linear; i.e., $n_e \simeq 40$ –5000 cm^{-3} (e.g., Osterbrock & Ferland 2006; Kewley et al. 2019).

(e.g., Groves et al. 2008; Krumholz & Matzner 2009; Kaasinen et al. 2017; Jiang et al. 2019). Finally, it has been suggested that galaxies or regions with higher Σ_{SFR} may have a larger fraction of young H II regions that are still overpressured with respect to their surroundings (e.g., Herrera-Camus et al. 2016; Jiang et al. 2019). It is important to note that while any of these scenarios could potentially explain a link between the level of star formation and the *volume-averaged* electron density, the relationship between $n_e(\text{rms})$ and $n_e([\text{S II}])$ as a function of redshift has not yet been established observationally, largely due to the difficulty in determining the average luminosities and volumes of unresolved H II regions.

Quantitative tests of these scenarios have also been hindered by the limited dynamic range of individual galaxy samples. Measurements of $n_e([\text{S II}])$ and $n_e([\text{O II}])$ in high- z galaxies have large associated uncertainties because the [S II] and [O II] emission lines are relatively weak, and the [O II] doublet lines can be significantly blended in galaxies with large integrated line widths. In addition, the measurements could be biased by emission from ionized gas outflows, which are prevalent at high- z . The line-emitting gas in star formation driven outflows at $z \sim 2$ is $\sim 5 \times$ denser than the line-emitting gas in the H II regions of the galaxies driving the outflows (e.g., Förster Schreiber et al. 2019). To recover intrinsic correlations between galaxy properties and the electron densities in H II regions, and to place stronger constraints on the physical driver(s) of the n_e evolution, it is necessary to assemble a large sample of galaxies spanning a wide range in redshift and galaxy properties, while also minimizing the degree of contamination from line emission produced outside of H II regions.

In this paper, we use a sample of 611 galaxies with no evidence of AGN activity or broad-line emission associated with outflows, drawn primarily from the KMOS^{3D} (Wisnioski et al. 2015, 2019) and SAMI (Bryant et al. 2015; Scott et al. 2018) integral field surveys, to investigate the physical processes driving the evolution of the typical electron density in SFGs from $z \sim 2.6$ to $z \sim 0$. The KMOS^{3D} sample is distributed across three redshift bins at $z \sim 0.9$, $z \sim 1.5$, and $z \sim 2.2$, allowing us to examine the evolution of n_e over ~ 5 Gyr of cosmic history with a single data set. We apply the same sample selection, spectral extraction, and stacking methodology to the SAMI sample to obtain a self-consistent measurement of n_e at $z \lesssim 0.1$. The combined sample is centered on the star-forming MS at each redshift and spans more than three orders of magnitude in SFR.

The paper is structured as follows. In Section 2, we outline the properties of our galaxy samples and describe the methods used to stack spectra, measure the [S II] doublet ratio, and calculate the H II region electron densities and pressures. We present our results on the redshift evolution of $n_e([\text{S II}])$, $n_e(\text{rms})$, and ionized gas filling factors in Section 3 and explore how $n_e([\text{S II}])$ varies as a function of global galaxy properties in Section 4. In Section 5, we compare our density measurements to quantitative predictions for various potential drivers of the n_e evolution and evaluate the most likely causes of the elevated electron densities in SFGs at high z . Our conclusions are summarized in Section 6.

Throughout this work, we assume a flat Λ CDM cosmology with $H_0 = 70 \text{ km s}^{-1} \text{ Mpc}^{-1}$ and $\Omega_0 = 0.3$. All galaxy properties have been derived assuming a Chabrier (2003) initial mass function.

2. Data and Methodology

2.1. KMOS^{3D} + Parent Sample

The high- z SFG sample used in this paper is primarily drawn from the KMOS^{3D} survey, a VLT/KMOS IFU survey focused on investigating the emission-line properties of primarily mass-selected galaxies at $0.6 < z < 2.7$ (Wisnioski et al. 2015, 2019). The KMOS^{3D} sample was drawn from the subset of 3D-HST galaxies with $\log(M_*/M_\odot) > 9$ and $K_{\text{AB}} \leq 23$ mag, with the aim to achieve a homogeneous coverage of the star-forming population as a function of stellar mass and redshift. In this paper, we focus on the subset of 525 KMOS^{3D} galaxies that were included in the Förster Schreiber et al. (2019) study of outflows across the high- z galaxy population. These objects were selected to have H α emission detected at a signal-to-noise ratio (S/N) per spectral channel > 3 , and no strong telluric line contamination in the region around the [N II] + H α complex. Förster Schreiber et al. (2019) visually inspected the spectra of all galaxies to search for broad emission-line components indicative of outflows, allowing us to isolate a sample of galaxies with no evidence of outflows for our analysis (see Section 2.3).

We supplement our KMOS^{3D} sample with galaxies from other high- z surveys that were also included in the Förster Schreiber et al. (2019) analysis. Forty-seven galaxies were drawn from the SINS/zC-SINF Survey (Förster Schreiber et al. 2009, 2018; Mancini et al. 2011), a VLT/SINFONI survey of 84 galaxies at $1.5 < z < 2.5$ selected on the basis of having secure spectroscopic redshifts and expected H α fluxes $\geq 5 \times 10^{-17} \text{ erg s}^{-1} \text{ cm}^{-2}$. Again, objects with low H α S/N or bad telluric contamination were excluded. Finally, we included six galaxies at $2 < z < 2.5$ from the K -band-selected sample of Kriek et al. (2007, 2008) observed with VLT/SINFONI and Gemini/GNIRS, and the galaxy EGS-13011166 at $z \sim 1.5$ observed with LBT/LUCI (Genzel et al. 2013, 2014). Our combined high- z parent sample consists of 579 galaxies, of which $\sim 90\%$ are drawn from KMOS^{3D}, and therefore this sample is henceforth referred to as the KMOS^{3D} + parent sample.

The gray histogram in the left-hand panel of Figure 1 shows the redshift distribution of the KMOS^{3D} + parent sample. The galaxies are grouped in three distinct redshift slices, corresponding to the redshift ranges where H α falls into the KMOS YJ ($z \sim 0.9$), H ($z \sim 1.5$), and K ($z \sim 2.2$) band filters.

Stellar masses were derived for all galaxies using population synthesis modeling of the rest-UV to optical/near-IR spectral energy distributions (SEDs), and SFRs were calculated from the rest-frame UV + IR luminosities using standard procedures, as described in Wuyts et al. (2011). Galaxy stellar disk effective radii (R_e) were derived from two-dimensional Sérsic fits to Hubble Space Telescope (HST) H -band imaging (van der Wel et al. 2012; Lang et al. 2014). The properties of the KMOS^{3D} and SINS/zC-SINF galaxies were taken directly from the survey papers, which adopted the methods described above (Förster Schreiber et al. 2009, 2018; Mancini et al. 2011; Tacchella et al. 2015; Wisnioski et al. 2019).

2.2. Extracting Integrated Spectra

Integrated spectra for the KMOS^{3D} and SINS/zC-SINF galaxies were extracted from the integral field data cubes as described in Section 2.5.1 of Förster Schreiber et al. (2019). Briefly, the data cubes were median subtracted to remove stellar continuum, 4σ clipped blueward and redward of the

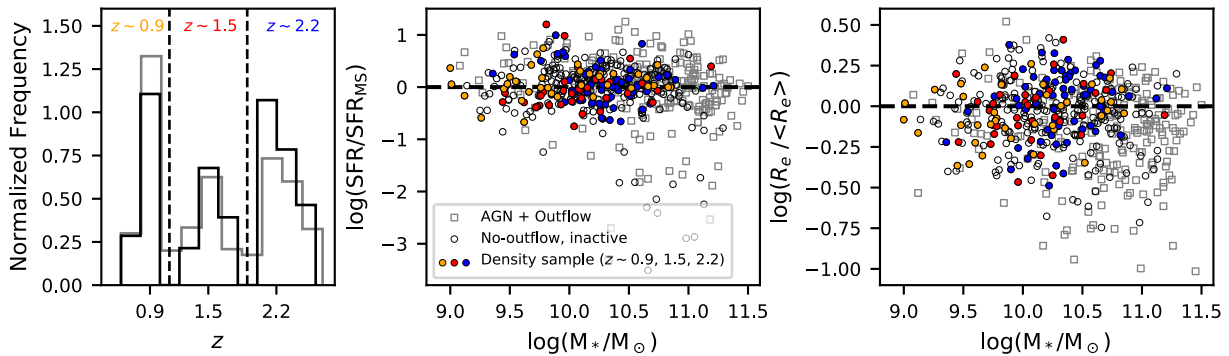


Figure 1. Left: normalized redshift distributions of the KMOS^{3D}+ parent sample (gray) and our density sample (black). Center and right: distribution of our density sample (solid markers) in offset from the star-forming MS (center) and offset from the van der Wel et al. (2014) galaxy mass–size relation (right), both as a function of stellar mass, compared to the distribution of the parent no-outflow inactive (open black circles) and AGN + outflow (open gray squares) samples. Orange, red, and blue markers indicate galaxies in the $z \sim 0.9$, $z \sim 1.5$, and $z \sim 2.2$ redshift slices, respectively.

strong emission lines to mask sky-line residuals, and smoothed over the spatial dimensions using a Gaussian kernel with a typical FWHM of 3 pixels for the KMOS cubes ($0''.6$) and 3–4 pixels for the SINFONI cubes ($0''.4$ – $0''.5$ for the seeing-limited data sets and $0''.15$ – $0''.2$ for the adaptive optics assisted observations), comparable to the typical FWHM of the point-spread function in all cases. A single Gaussian line profile was fit to the H α emission in each spaxel of the smoothed cubes to create velocity field maps, and the velocity field maps were used to shift the (unsmoothed) spectra of all spaxels within each galaxy to the same velocity centroid. The velocity shifting minimizes broadening of the integrated emission-line profiles induced by the presence of large-scale, gravitationally driven line-of-sight velocity gradients across rotating disks. Integrated spectra were extracted by summing the velocity-shifted spectra of all spaxels within a galactocentric radius of $0''.25$ – $0''.6$ (corresponding to a physical aperture radius of 2–5 kpc, similar to the median R_e of 3.4 kpc), where the aperture size was adjusted based on the galaxy size to optimize the S/N of the extracted spectrum.

2.3. Selection of the KMOS^{3D}+ Density Sample

In this work, we focus on star-forming galaxies with no evidence of AGN activity or broad-line emission indicative of outflows. Förster Schreiber et al. (2019) created a single stacked spectrum of inactive galaxies with strong outflows spanning $0.6 < z < 2.6$ and measured the [S II] ratios and electron densities of the narrow ISM component and the broader outflow component individually. They found that the outflowing gas is significantly denser than the ISM material (see also Arribas et al. 2014; Ho et al. 2014; Perna et al. 2017; Kakkad et al. 2018; Fluetsch et al. 2020), suggesting that the ISM material may be shocked and compressed as it is swept up by the hot wind fluid.

In principle, the typical n_e in SFGs at each redshift could be measured by stacking the spectra of all galaxies (with and without outflows) and measuring the [S II] ratio in the narrow-line component. We construct such stacks for each redshift slice of the KMOS^{3D}+ sample, but in the $z \sim 0.9$ and $z \sim 1.5$ stacks, the S/N of the broad outflow component is not sufficient to permit a robust two-component decomposition of the emission-line profiles (see Appendix A.1). If we fit only one kinematic component to each of the [S II] lines, the measured electron density would be a line-flux-weighted

average of the ISM density and the outflow density. Therefore, we remove galaxies with outflows prior to stacking. The potential impact of this choice on the measured electron densities is discussed at the end of this section.

AGN host galaxies are removed because (1) outflows are prevalent in AGN host galaxies (e.g., Förster Schreiber et al. 2014, 2019; Genzel et al. 2014; Harrison et al. 2016; Leung et al. 2019), and (2) we calculate the electron density using H II region photoionization models (discussed in Section 2.6), which cannot be applied to the spectra of AGN host galaxies because the AGN ionizing radiation field is significantly harder than an O-star spectrum and will produce a very different ionization and temperature structure (see, e.g., discussion in Kewley et al. 2019; Davies et al. 2020).

Förster Schreiber et al. (2019) classified all galaxies in the KMOS^{3D}+ sample as either AGN or inactive, and outflow or no-outflow. Galaxies were classified as AGN if their hard X-ray luminosity, radio luminosity, mid-IR colors, or [N II]/H α ratio exceeded the threshold for pure star formation. Outflows were identified visually based on the presence of broad or asymmetric features in the integrated emission-line profiles. The velocity shifting that was performed prior to spectral extraction increases the sharpness and S/N per spectral channel of the line emission from the galaxy disk (see, e.g., Figure 1 of Swinbank et al. 2019) and therefore maximizes the outflow detection fraction by pushing the detection limit to lower outflow velocities and mass outflow rates. The majority (356/579 or 61%) of the galaxies were classified as inactive with no visually identifiable outflow component in the line emission (“no outflow”). A further 87 galaxies (15%) were classified as inactive with outflows, and the remaining 136 (23%) galaxies were classified as AGN hosts (of which 94, or 16% of the parent sample, have detected outflows).

Of the 356 inactive galaxies with no outflows, 320 have spectra covering the [S II] doublet. The [S II] emission lines are relatively weak (with a typical peak amplitude $\sim 5\%$ that of the H α line at $z \sim 1$ –2), and small changes in the [S II] $\lambda 6716$ /[S II] $\lambda 6731$ ratio correspond to relatively large differences in the derived electron density, so it is very important to create a sample of spectra without significant sky contamination in the [S II] doublet region. We visually inspected the spectra of all 320 no-outflow inactive galaxies and removed objects with elevated errors or bad systematics in the [S II] region. This quality cut leaves us with a final sample of 140 galaxies (the “density sample”).

The black histogram in the left-hand panel of Figure 1 shows the redshift distribution of the density sample. Of our 140 galaxies, 39 galaxies fall in the $z \sim 0.9$ slice, 36 galaxies fall in the $z \sim 1.5$ slice, and 65 galaxies fall in the $z \sim 2.2$ slice. The density sample covers a wide redshift range and allows us to probe the n_e evolution over ~ 5 Gyr in cosmic history with consistent data and analysis.

The center and right-hand panels of Figure 1 show how the galaxies are distributed in the M_* -SFR (center) and M_* - R_e (right) planes. We have removed the average trends in SFR and R_e as a function of stellar mass and redshift, adopting the Speagle et al. (2014) parameterization of the star-forming MS (their Equation (28); chosen for consistency with the Tacconi et al. 2020 molecular gas depletion time scaling relation, which is later used to estimate molecular gas masses) and the van der Wel et al. (2014) mass-size relation for late-type galaxies as a function of the Hubble parameter $H(z)$. The filled circles show the density sample (orange: $z \sim 0.9$, red: $z \sim 1.5$, blue: $z \sim 2.2$), the open circles show the no-outflow inactive galaxies that did not pass the visual inspection cut, and the open gray squares show galaxies with outflows and/or AGN activity.

The density sample probes typical SFGs spanning ~ 2 dex in both M_* and sSFR, and has a median stellar mass of $\log(M_*/M_\odot) = 10.2$, with a slight trend toward higher stellar masses at higher redshift (the median stellar masses in the individual redshift bins are $\log(M_*/M_\odot) = 9.9$ at $z \sim 0.9$, $\log(M_*/M_\odot) = 10.1$ at $z \sim 1.5$, and $\log(M_*/M_\odot) = 10.3$ at $z \sim 2.2$). By nature of the selection criteria, the density sample does not extend to the highest stellar masses or into the compact, quiescent, and starburst galaxy regimes where AGNs and outflows are most frequent (see Förster Schreiber et al. 2019). The removal of the highest stellar mass objects, which also have the highest SFRs, means that the density sample has a slightly lower median SFR than the parent sample at fixed z . The most actively star-forming galaxies are expected to have the highest n_e (e.g., Shimakawa et al. 2015; Kaasinen et al. 2017; Jiang et al. 2019; Kashino & Inoue 2019) and therefore there is a possibility that the electron densities measured from the density sample could underestimate the true average n_e in H II regions at each redshift. However, we perform a test that suggests that the n_e values measured from our density sample are likely to reflect the average gas conditions in H II regions across the wider SFG population (see full description in Appendix A.1).

2.4. $z \sim 0$ Comparison Sample: SAMI Galaxy Survey

We measure the zero point of the n_e evolution using a sample of galaxies from the SAMI Galaxy Survey (Bryant et al. 2015), an integral field survey of ~ 3000 galaxies at $z \lesssim 0.1$. We choose an IFU sample rather than the much larger set of SDSS fiber spectra because the IFU data can be analyzed using exactly the same methods applied to the KMOS^{3D}+ data, allowing us to obtain a self-consistent measurement of n_e at $z \sim 0$. We specifically choose the SAMI survey because (1) it is mass selected and (2) the spectral resolution ($R \sim 4300$) is similar to that of our KMOS^{3D}+ data ($R \sim 3500$ – 4000). In comparison, the spectral resolution of the MaNGA survey is $R \sim 2000$ (Bundy et al. 2015).

The most recent data release (DR2) includes blue and red data cubes (covering 3750–5750 Å and 6300–7400 Å observed, respectively) for 1559 galaxies and velocity maps for 1526/1559 galaxies (Scott et al. 2018). We start with 1197

galaxies that lie in the same stellar mass range as our KMOS^{3D}+ targets ($\log(M_*/M_\odot) = 9.0$ – 11.2). Using the published emission-line catalogs, we select 839 galaxies for which H α is detected at $\geq 10\sigma$ and H β , [N II] $\lambda 6584$ and [O III] $\lambda 5007$ are all detected at $\geq 3\sigma$. We remove 280 galaxies with significant contributions from nonstellar sources (lying above the Kauffmann et al. 2003 classification line on the [N II]/H α versus [O III]/H β diagnostic diagram). For each of the remaining 559 galaxies, we velocity-shift the blue and red data cubes, masking out spaxels for which no velocity measurement could be obtained, and then sum the velocity-shifted cubes along both spatial dimensions to produce integrated spectra,¹⁷ as described in Section 2.2. Stellar continuum fitting and subtraction is performed by running the Penalized Pixel-Fitting method (Cappellari & Emsellem 2004; Cappellari 2017) on the full (blue + red) spectrum for each galaxy, using the MILES library of stellar templates (Vazdekis et al. 2010). The blue spectra are only used to constrain the continuum fitting and are not used in any further analysis. We visually inspect all integrated spectra and continuum fits, and reject galaxies with strong sky-line residuals near any of the primary emission lines (H α , [N II] and [S II]), evidence for outflow emission (broad or asymmetric emission in multiple lines), or bad continuum fits. The final sample consists of 471 galaxies.

We calculate the global SFRs of the SAMI galaxies by summing the publicly available dust-corrected H α SFR maps (described in Medling et al. 2018). The left-hand panel of Figure 2 shows how the SAMI galaxies are distributed in the M_* -SFR plane. The SAMI sample spans ~ 2 dex in M_* and ~ 3.5 dex in sSFR, and has a median stellar mass of $\log(M_*/M_\odot) = 9.6$, significantly lower than the median stellar mass of the KMOS^{3D}+ sample ($\log(M_*/M_\odot) = 10.2$) despite covering the same stellar mass range. The differences between the median stellar masses of the samples are accounted for when relevant to our analysis.

The red dotted line in Figure 2 shows the Speagle et al. (2014) star-forming MS. The SAMI galaxies follow a slightly steeper relation indicated by the red dashed line, which is the best fit to the full sample of galaxies with $\log(\text{sSFR} [\text{yr}^{-1}]) > -11.2$ (the approximate boundary between the star-forming and quiescent populations). The discrepancy in the MS slope is attributed to the fact that spaxels with significant contributions from nonstellar excitation sources are masked in the SAMI SFR maps, meaning that the calculated SFRs are lower limits (Medling et al. 2018). Throughout the paper, the MS offset of the SAMI galaxies is defined with respect to the best-fit (red dashed) line.

The effective radii of the SAMI galaxies were derived from two-dimensional Sérsic fits to the GAMA r -band imaging (Kelvin et al. 2012). The right-hand panel of Figure 2 shows where the SAMI galaxies lie in the M_* - R_e plane, compared to the $z \sim 0$ extrapolation of the van der Wel et al. (2014) mass-size relation (red dashed line) which has been adjusted to the rest-frame central wavelength of the SDSS r -band filter ($\lambda \simeq 6020$ Å) using their Equation (1). The SAMI galaxies follow the expected increase in average size with increasing stellar mass but are $\sim 10\%$ smaller than predicted by the van der Wel et al. (2014) relation.

¹⁷ The unmasked spaxels cover a median galactocentric radius of $\sim 2R_e$. This is larger than the typical radius covered by the KMOS^{3D}+ spectra, but excluding spaxels outside $1 R_e$ does not have any significant impact on the electron densities measured from the SAMI spectra.

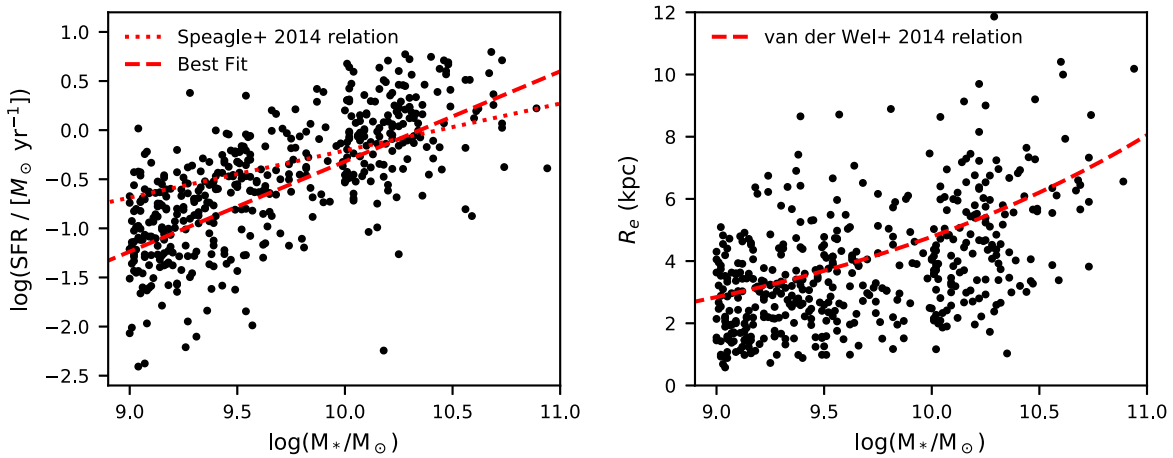


Figure 2. Distribution of SAMI galaxies in the (left) M_* -SFR and (right) M_* - R_e planes. The red dashed line in the right-hand panel shows the $z \sim 0$ extrapolation of the van der Wel et al. (2014) mass-size relation, which has been adjusted to the rest-frame central wavelength of the SDSS r -band filter ($\lambda \simeq 6020 \text{ \AA}$) using their Equation (1).

2.5. Stacking

We stack the integrated spectra of different sets of galaxies to produce high-S/N composite spectra that can be used to make robust measurements of the [S II] ratio, n_e , and thermal pressure. Before stacking, each spectrum is normalized to prevent the measured [S II] ratios from being strongly biased toward galaxies with brighter line emission (i.e., galaxies at lower redshifts and/or with higher SFRs). The most accurate estimate of the average [S II] ratio would be obtained by normalizing each spectrum to the peak amplitude of the [S II] $\lambda 6731$ line, because this would, in the case of infinite S/N, yield the same result as measuring the [S II] ratios of all galaxies individually and averaging the results. However, neither of the [S II] lines is robustly detected in all of the galaxies. Instead, we normalize to $H\alpha$, which removes the majority of the variation in the [S II] $\lambda 6731$ line amplitude because the SFR (which scales linearly with the $H\alpha$ luminosity) varies by two to three orders of magnitude within each redshift slice, whereas the [S II]/ $H\alpha$ ratios of galaxies with H II-region-like spectra typically vary by only a factor of $\lesssim 5$ at fixed redshift (e.g., Kewley et al. 2006; Kashino et al. 2017; Shapley et al. 2019).

The normalized galaxy spectra are averaged to obtain the stacked spectrum. When averaging, values lying more than 3σ away from the median in each spectral channel are masked to ensure that the final stacks are not disproportionately affected by any possible remaining outliers.

2.6. Electron Density and Thermal Pressure Calculations

2.6.1. [S II] $\lambda 6716$ /[S II] $\lambda 6731$ Ratio and Model Grids

We measure the electron density and the thermal pressure from each stacked spectrum using the [S II] $\lambda 6716$ /[S II] $\lambda 6731$ ratio (also referred to as the “[S II] ratio” and “ $R_{S II}$ ”). [S II] $\lambda 6716$ and [S II] $\lambda 6731$ originate from excited states that have similar excitation energies but different collision strengths and radiative decay rates, meaning that the [S II] ratio is strongly dependent on n_e but only weakly dependent on temperature. In the low-density limit, the timescale for collisional de-excitation is significantly longer than the timescale for radiative decay and the population ratio is determined by the ratio of the collision

strengths, resulting in $R_{S II} \sim 1.45$. In the high-density limit, collisions govern transitions between the states, and the electrons are distributed in a Boltzmann population ratio, resulting in $R_{S II} \sim 0.45$. At densities similar to the critical density (where the probability of collisional de-excitation and radiative decay are approximately equal), $R_{S II}$ varies almost linearly with n_e . The [S II] ratio is most sensitive to densities in the range ~ 40 – 5000 cm^{-3} (e.g., Osterbrock & Ferland 2006; Kewley et al. 2019) and is therefore a good probe of the electron density in the line-emitting material within H II regions, which typically ranges from tens to hundreds cm^{-3} .

We convert from $R_{S II}$ to electron density and thermal pressure using the constant-density and constant-pressure model grids presented in Kewley et al. (2019), respectively. The grids are outputs of plane-parallel H II region models run with the MAPPINGS 5.1 photoionization code. The constant-density models allow for a radially varying temperature and ionization structure within the nebula, and the constant-pressure models additionally allow for radially varying density structure. Real H II regions can have strong density gradients (e.g., Binette et al. 2002; Phillips 2007) but are expected to have approximately constant pressure (e.g., Field 1965; Begelman 1990), and therefore, the pressure provides a more meaningful description of the conditions within H II regions than the electron density.¹⁸

Outputs of the constant-density and constant-pressure models are provided for $\log(n_e/\text{cm}^{-3}) = 1.0$ – 5.0 and $\log(P/k) = 4.0$ – 9.0 , respectively, with a sampling of 0.5 dex in both quantities. Throughout this paper, P/k is in units of K cm^{-3} . For each value of n_e and $\log(P/k)$, the grids include outputs of models run at five metallicities ($12 + \log(\text{O}/\text{H}) = 7.63, 8.23, 8.53, 8.93, \text{ and } 9.23$) and nine ionization parameters ($\log q = 6.5$ – 8.5 in increments of 0.25 dex). The metallicity and ionization parameter determine the temperature structure of the nebula. The [S II] ratio has a weak dependence on electron temperature because the collisional de-excitation rate scales with $T^{-1/2}$ (from the Maxwell-Boltzmann

¹⁸ We note that the electron densities derived from the outputs of the self-consistent H II region photoionization models described here are generally in very good agreement with electron densities derived using model atom calculations that assume constant temperature and ionization structure, provided that the input atomic data are the same (Kewley et al. 2019).

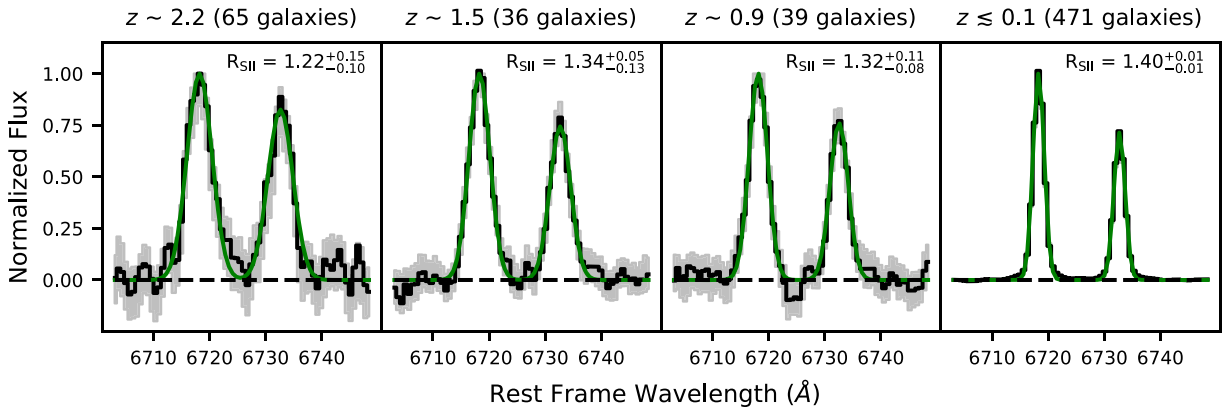


Figure 3. Stacked [S II] doublet profiles of galaxies with no evidence for outflows or AGN activity, in four redshift slices: $1.9 \lesssim z \lesssim 2.6$, $1.1 \lesssim z \lesssim 1.9$, $0.6 \lesssim z \lesssim 1.1$, and $z \lesssim 0.1$. The gray shaded regions indicate the 1σ spread of the 600 bootstrap stacks generated for each redshift slice (described in Section 2.6.2). The green curves indicate the best-fit Gaussian profiles.

electron temperature distribution), and therefore, the critical density scales with $T^{1/2}$ (e.g., Dopita & Sutherland 2003; Kewley et al. 2019).

2.6.2. Measurements

We derive $n_e([\text{S II}])$ and $\log(P_{\text{th}}/k)([\text{S II}])$ for each stacked spectrum by interpolating the model grids in q , Z , and $R_{\text{S II}}$. The [S II] ratio is measured by fitting a single Gaussian to each of the [S II] lines. We require both lines to have the same velocity centroid and velocity dispersion.

We estimate the average metallicity of the galaxies in each stack using the [N II]+ [S II]+ H α calibration from Dopita et al. (2016). This diagnostic is relatively insensitive to variations in the density/pressure and ionization parameter, making it well suited for use with high-redshift galaxies. Dopita et al. (2016) calibrated the diagnostic using MAPPINGS 5.0 H II region models run with the same abundance set as the Kewley et al. (2019) models, which is crucial because of the large systematic discrepancies between different metallicity calibrations in the literature. We simultaneously fit all of the strong emission lines ([N II] λ 6548, H α , [N II] λ 6584, [S II] λ 6716, [S II] λ 6716) to measure the [N II]/H α and [S II]/H α ratios and obtain an estimate of the metallicity. The metallicity estimates for the KMOS^{3D}+ stacks are listed in Table 4.

Our high- z spectra do not cover the [O III] λ 5007 and [O II] λ λ 3726,3729 emission lines, which are required to make a direct measurement of the ionization parameter. We adopt typical ionization parameters of $\log(q) = 7.8$ for the KMOS^{3D}+ galaxies based on measurements of star-forming galaxies at $z \sim 1$ –2 from the COSMOS-[O II] and MOSDEF surveys (Sanders et al. 2016; Kaasinen et al. 2018), and $\log(q) = 7.3$ for the SAMI galaxies (Poetrodjojo et al. 2018). However, varying the ionization parameter by a factor of 3 changes the derived pressures and densities by at most 0.1 dex (a factor of 1.2), and therefore, the choice of ionization parameter has a minimal impact on our results.

We estimate the errors on the derived $R_{\text{S II}}$, $n_e([\text{S II}])$ and $\log(P_{\text{th}}/k)([\text{S II}])$ values using a combination of bootstrapping and Monte Carlo sampling to account for both sample variance and measurement uncertainties. For a given stack of N galaxies, we randomly perturb the spectrum of each galaxy by its measurement errors, draw N perturbed spectra allowing for duplicates (bootstrapping), stack the drawn spectra, and measure $R_{\text{S II}}$, $n_e([\text{S II}])$ and $\log(P_{\text{th}}/k)([\text{S II}])$. This process is

repeated 600 times,¹⁹ and the 16th and 84th percentile values of the 600 measurements of $R_{\text{S II}}$, $n_e([\text{S II}])$ and $\log(P_{\text{th}}/k)([\text{S II}])$ are taken as the lower and upper boundaries of the 1σ confidence interval for each quantity. We note that due to the relatively high S/N of the input spectra, the error budget is dominated by sample variance in all cases.

3. Redshift Evolution of H II Region Electron Densities

3.1. Typical [S II] Electron Density at $z \sim 0.9$, $z \sim 1.5$, and $z \sim 2.2$ with KMOS^{3D}+

We begin by using our “density sample” of inactive galaxies with no outflows to measure the average $n_e([\text{S II}])$ and $\log(P_{\text{th}}/k)([\text{S II}])$ in each of the KMOS^{3D}+ redshift slices. The stacked [S II] doublet profiles and best Gaussian fits are shown in Figure 3. The gray shaded regions indicate the 1σ spread of the 600 bootstrap stacks generated for each redshift slice.

The left-hand panel of Figure 4 illustrates how the measured [S II] ratios are converted to electron densities. For each redshift slice, we interpolate the q - Z - n_e - $R_{\text{S II}}$ photoionization model output grid at the measured Z and adopted q to produce a set of $(n_e, R_{\text{S II}})$ pairs, plotted as gray circles. The gray dashed lines are linear interpolations between the sampled electron densities. We generate and plot the circles and lines for each stack individually, but the differences between the sets of interpolated outputs are barely visible. The green stars and error bars show the $R_{\text{S II}}$ measurements for the KMOS^{3D}+ stacks and the corresponding $n_e([\text{S II}])$ values derived from the outputs of the constant-density models. The $\log(P_{\text{th}}/k)([\text{S II}])$ values are derived from the outputs of the constant-pressure models using the same method. All of the measured and derived quantities are listed in Table 4.

We find $n_e([\text{S II}]) = 101_{-85}^{+59} \text{ cm}^{-3}$ at $z \sim 0.9$, consistent with results from the KROSS survey (Swinbank et al. 2019), and $n_e([\text{S II}]) = 79_{-40}^{+120} \text{ cm}^{-3}$ at $z \sim 1.5$, in agreement with measurements from the COSMOS-[O II] (Kaasinen et al. 2017) and FMOS-COSMOS (Kashino et al. 2017) surveys. At $z \sim 2.2$, we measure $n_e([\text{S II}]) = 187_{-132}^{+140} \text{ cm}^{-3}$, similar to the values reported by the KBSS-MOSFIRE (Steidel et al. 2014) and MOSDEF (Sanders et al. 2016) surveys.

¹⁹ This number was empirically verified to result in consistent error estimates between trials.

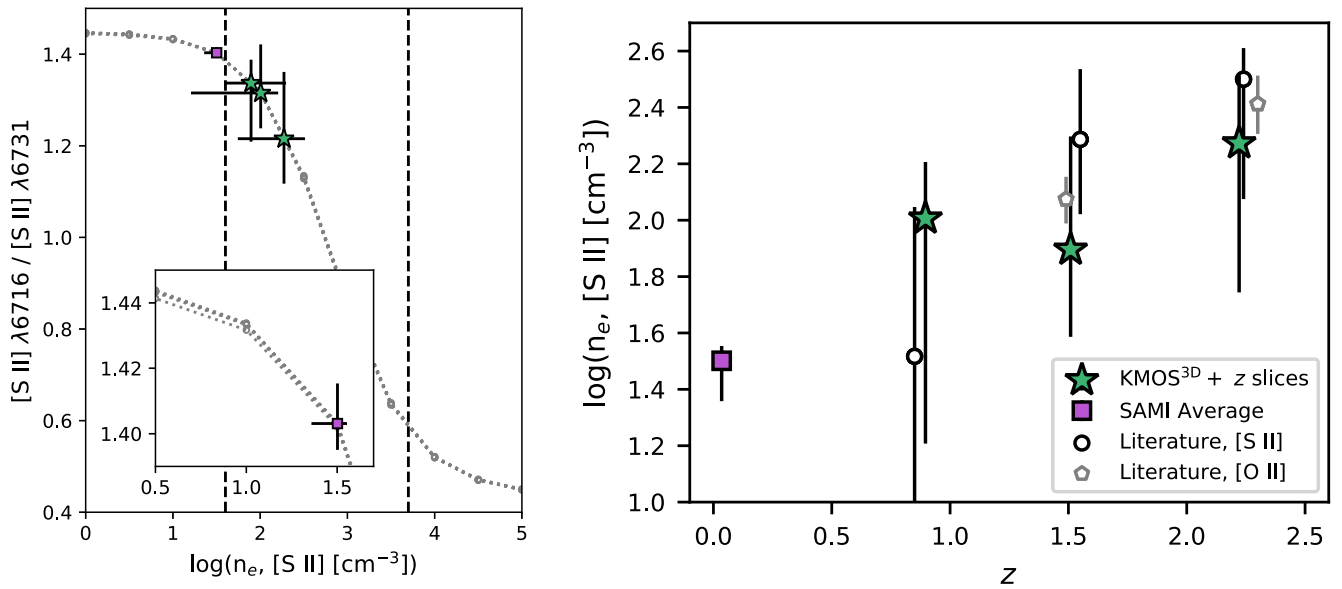


Figure 4. Left: illustration of the conversion between $R_{S\text{ II}}$ and $n_e([S\text{ II}])$. For each redshift slice, we interpolate the q - Z - n_e - $R_{S\text{ II}}$ photoionization model output grid at the measured Z and adopted q to produce a set of $(n_e, R_{S\text{ II}})$ pairs. The $(n_e, R_{S\text{ II}})$ pairs are plotted as open gray circles, and the gray dashed lines are linear interpolations between the sampled electron densities. We generate and plot the circles and lines for each stack individually but the differences between the four sets of interpolated outputs are barely visible. Black dashed lines indicate the boundaries of the region where $R_{S\text{ II}}$ is most sensitive to n_e . The green stars and purple square show the measured $R_{S\text{ II}}$ and the derived $n_e([S\text{ II}])$ for the KMOS^{3D}+ and SAMI stacks, respectively. The inset in the bottom left is a zoom-in on the region around the SAMI measurement, showing that the measured $R_{S\text{ II}}$ is inconsistent with the theoretical maximum value. Right: the redshift evolution of $n_e([S\text{ II}])$ based on the combination of the KMOS^{3D}+, SAMI and high- z literature ([S II]: black circles, [O II]: gray pentagons) samples.

The choice to remove galaxies with outflows from our sample was motivated by the observation of enhanced electron densities in outflowing material (Förster Schreiber et al. 2019). However, the electron densities measured from our sample of no-outflow inactive galaxies match the electron densities measured from other galaxy samples that likely include star formation driven outflows. This suggests that the increased incidence of outflows at high redshift does not have a significant impact on the magnitude of the density evolution inferred from single-component Gaussian fits to the [S II] doublet lines. In Appendix A.2, we confirm that including sources with star formation driven outflows (in proportion to their population fraction) has a minimal impact on the measured average densities.

We also investigate the impact of AGN contamination on the measured densities. Uniform identification of AGN host galaxies at high redshift is challenging due to the varying availability and depth of multiwavelength ancillary data between extragalactic deep fields. In Appendix A.3, we present tentative evidence to suggest that the measured densities could be up to a factor of ~ 2 larger when AGN host galaxies are included.

3.2. Typical [S II] Electron Density at $z \sim 0$

We use the velocity-shifted spectra of the sample of 471 SAMI galaxies to obtain a self-consistent measurement of the electron density at $z \sim 0$. The stacked [S II] doublet profile and best Gaussian fit are shown in the rightmost panel of Figure 3. The purple square in the left-hand panel of Figure 4 indicates that the SAMI stack lies in the low- n_e regime of the [S II] diagnostic where $R_{S\text{ II}}$ asymptotes toward the theoretical maximum value, causing the n_e - $R_{S\text{ II}}$ curve to become quite flat. However, the inset shows that due to the very high S/N of the stacked spectrum, the measured $R_{S\text{ II}}$ is inconsistent with the

theoretical maximum value at the $\sim 5\sigma$ level, implying that we have a reliable measurement of n_e .

The measured $R_{S\text{ II}}$ corresponds to an electron density of $n_e([S\text{ II}]) = 32_{-9}^{+4} \text{ cm}^{-3}$. This value is in very good agreement with electron densities measured for resolved regions of local spiral galaxies using the $[N\text{ II}]122 \mu\text{m}/[N\text{ II}]205 \mu\text{m}$ ratio, which is a robust tracer of electron density down to $n_e \sim 10 \text{ cm}^{-3}$ (Herrera-Camus et al. 2016), and with the typical $n_e([S\text{ II}])$ derived from stacked SDSS fiber spectra of local galaxies (Kashino & Inoue 2019).

3.3. Redshift Evolution of the [S II] Electron Density and the Impact of Diffuse Ionized Gas

We combine the SAMI and KMOS^{3D}+ measurements to investigate how n_e evolves as a function of redshift, as shown in the right-hand panel of Figure 4. We also gather [S II] and [O II] ratio measurements from other surveys of high- z galaxies in the literature (KBSS-MOSFIRE, Steidel et al. 2014; MOSDEF, Sanders et al. 2016; KROSS, Stott et al. 2016; COSMOS-[O II], Kaasinen et al. 2017; and FMOS-KMOS, Kashino et al. 2017). We require that the median SFR of each sample lies within 0.5 dex of the star-forming MS to ensure that the galaxies are representative of the underlying SFG population at the relevant redshifts. The majority of the literature measurements are based on slit spectra with the exception of the data from KROSS, a KMOS IFU survey of SFGs at $0.6 < z < 1.0$ (Stott et al. 2016). A more complete description of the literature samples is given in Appendix B. We recalculate the electron densities from the published line-ratio measurements to avoid systematic biases in the conversion between line ratios and n_e arising from differences in atomic data or assumed electron temperature (see, e.g., discussions in Sanders et al. 2016 and Kewley et al. 2019).

We do not calculate $\log(P_{\text{th}}/k)([\text{S II}])$ for the literature samples because we do not have the line-ratio measurements required to obtain self-consistent metallicity estimates.

The [S II] and [O II] lines originate from different regions of the nebula and will only give consistent densities if the electron temperature does not vary significantly between the [S II]- and [O II]-emitting regions. Sulfur exists as S^+ for photon energies in the range 10.4–23.3 eV,²⁰ and therefore, [S II] emission is expected to originate primarily from dense clumps and the partially ionized zone at the edge of the H II region (e.g., Proxauf et al. 2014). On the other hand, O^+ exists for photon energies in the range 13.6–35.1 eV, and therefore, [O II] is emitted over a much larger fraction of the H II region (Kewley et al. 2019). However, Sanders et al. (2016) showed that there is a good correspondence between the global [S II] and [O II] densities measured for star-forming galaxies at $z \sim 2$. In our plots, we distinguish between densities measured from the [S II] ratio (circles with black outlines) and the [O II] ratio (pentagons with gray outlines).

Figure 4 clearly suggests that the typical electron densities inferred from the [S II] and [O II] doublet ratios have decreased by a factor of ~ 6 –10 over the last 10 Gyr, consistent with previous studies. However, to understand whether this reflects an evolution in the typical properties of ionized gas inside H II regions, we must consider the origin of the line emission. It is well established that around 50% of the $\text{H}\alpha$ emission from local galaxies originates from diffuse ionized gas (DIG) between H II regions (e.g., Thilker et al. 2002; Oey et al. 2007; Poetrodjojo et al. 2019; Chevance et al. 2020). The DIG is thought to be ionized by a combination of leaked ionizing photons from H II regions, radiation from low-mass evolved stars, and shock excitation (e.g., Martin 1997; Ramirez-Ballinas & Hidalgo-Gómez 2014; Zhang et al. 2017). DIG-dominated regions have larger [N II]/ $\text{H}\alpha$ and [S II]/ $\text{H}\alpha$ ratios than H II regions (e.g., Rand 1998; Haffner et al. 1999; Madsen et al. 2006), and it is therefore likely that a significant fraction of the [S II] emission from the SAMI galaxies is associated with the DIG rather than H II regions.

The line-emitting clumps in the DIG have a typical density of $n_e \sim 0.05 \text{ cm}^{-3}$ (e.g., Reynolds 1991), meaning that DIG contamination could potentially have a significant impact on the measured [S II] ratios. Fortunately, the [S II] ratio saturates for densities below $n_e \sim 40 \text{ cm}^{-3}$ (see the left-hand panel of Figure 4), such that the [S II] ratios measured for H II regions at or below this density will be relatively unimpacted by DIG contamination. Recent surveys of resolved H II regions in nearby spiral galaxies have found that the majority of H II regions have [S II] ratios in the low-density limit (e.g., Cedrés et al. 2013; Berg et al. 2015; Kreckel et al. 2019). In NGC 7793, the distributions of [S II] ratios in H II regions and the DIG are indistinguishable (Della Bruna et al. 2020). These results suggest that the impact of DIG contamination on the derived $n_e([\text{S II}])$ at $z \sim 0$ may be relatively small.

The situation is different at higher redshift where the measured electron densities are significantly above the low-density limit of the [S II] ratio. However, the fractional contribution of the DIG to the $\text{H}\alpha$ emission is anticorrelated with the $\text{H}\alpha$ surface brightness (e.g., Oey et al. 2007) and is predicted to decrease with increasing redshift until it becomes negligible at $z \sim 2$ (e.g., Sanders et al. 2017; Shapley et al. 2019,

and see discussion in the following section). We therefore assume that the measured electron density evolution shown in Figure 4 is most likely to reflect a change in the intrinsic $n_e([\text{S II}])$ of H II regions over cosmic time.

We note that even though DIG contamination is not expected to have a significant impact on the measured $R_{\text{S II}}$, the derived $n_e([\text{S II}])$ and $\log(P_{\text{th}}/k)([\text{S II}])$ do not reflect the average properties of gas in H II regions. Galaxies commonly display negative radial gradients in H II region electron density (e.g., Gutiérrez & Beckman 2010; Cedrés et al. 2013; Herrera-Camus et al. 2016) and metallicity (e.g., Zaritsky et al. 1994; Moustakas et al. 2010; Ho et al. 2015), the latter of which directly corresponds to positive electron temperature gradients because metal lines are the primary source of cooling in the 10^4 K ISM (e.g., Osterbrock & Ferland 2006). The derived $n_e([\text{S II}])$ and $\log(P_{\text{th}}/k)([\text{S II}])$ represent the line-flux-weighted average properties of the gas within each aperture and will therefore likely be biased toward the densest H II regions in the central regions of the galaxies.

3.4. Redshift Evolution of the Volume-averaged Electron Density and Ionized Gas Filling Factor

3.4.1. Background

The electron densities in H II regions can be measured using two complementary methods. The measurements presented thus far have been based on $R_{\text{S II}}$, a density-sensitive line ratio that probes the local n_e in the line-emitting material. The second approach is to use the $\text{H}\alpha$ luminosity, which is proportional to the volume emission measure, to calculate the rms number of electrons per unit volume, $n_e(\text{rms})$ (Equation (2)). The ratio of $n_e(\text{rms})$ to $n_e([\text{S II}])$ scales with the square root of the volume filling factor of the line-emitting material (Equation (5)).

There is some evidence to suggest that the rms electron densities (and by extension, the volume-averaged thermal pressures) of local H II regions may be approximately proportional to the external ambient pressure (e.g., Elmegreen & Hunter 2000; Gutiérrez & Beckman 2010), hinting that the local environment may play an important role in regulating H II region properties (e.g., Kennicutt 1984). Measurements of $n_e(\text{rms})$ therefore represent a crucial link in our understanding of how global galaxy properties impact the local electron density of the line-emitting material.

The spatial resolution of our integral field observations is far below what is required to resolve individual H II regions, and with our data, we can only estimate the rms number of electrons per unit volume on galactic scales. This provides a lower limit on the rms number of electrons per unit volume within the H II regions themselves, because H II regions do not fill the entire volumes of star-forming disks. The rms electron density within the H II regions is related to the measured $n_e(\text{rms})$ within R_e through the inverse of the volume ratio: $n_e(\text{rms}, \text{H II}) = n_e(\text{rms}, R_e) \times V_{R_e}/V_{\text{H II}}$. The same scaling applies to the volume filling factors.

We use the SAMI and KMOS^{3D} data sets to estimate $n_e(\text{rms})$ and the volume filling factor of the line-emitting gas within R_e at $z \sim 0, 0.9, 1.5,$ and 2.2 . These calculations require a measurement of the $\text{H}\alpha$ luminosity within R_e (described in Section 3.4.2) and an estimate of the disk scale height (discussed in Section 3.4.3).

²⁰ Ionization energies taken from the NIST Atomic Spectra Database (ver. 5.7.1); <https://physics.nist.gov/asd>.

3.4.2. $H\alpha$ Luminosities

The total $H\alpha$ luminosities within R_e for the KMOS^{3D} galaxies are derived from the published integrated $H\alpha$ fluxes (Kriek et al. 2007; Förster Schreiber et al. 2009, 2018; Wisnioski et al. 2019) as follows. The $H\alpha$ fluxes are corrected for extinction using the continuum A_V obtained from SED fitting and adopting the Wuyts et al. (2013) prescription for extra attenuation toward nebular regions. The $H\alpha$ and H -band (observed frame) effective radii of SFGs at $z \sim 1$ –2 are approximately equal (e.g., Nelson et al. 2016b; Förster Schreiber et al. 2018; Wilman et al. 2020), and therefore, we divide the integrated $H\alpha$ fluxes by 2 to obtain the fluxes within R_e . For the SAMI galaxies, we directly use the published $H\alpha$ fluxes and dust correction factors within R_e from the “recommend-component” emission-line-flux catalog (Scott et al. 2018). The $H\alpha$ and r -band sizes of the SAMI galaxies are typically consistent to within ~ 0.1 dex (Schaefer et al. 2017).

The $H\alpha$ emission includes contributions from both H II regions and DIG, as discussed in Section 3.3. To isolate the $H\alpha$ emission from H II regions, we assume that the fraction of $H\alpha$ emission associated with the DIG ($f_{H\alpha, \text{DIG}}$) follows the relationship calibrated by Sanders et al. (2017):

$$f_{H\alpha, \text{DIG}} = -1.5 \times 10^{-14} \left(\frac{\Sigma_{H\alpha}}{\text{erg s}^{-1} \text{kpc}^{-2}} \right)^{1/3} + 0.748. \quad (6)$$

This expression is the best fit to measurements of $\Sigma_{H\alpha}$ and $f_{H\alpha, \text{DIG}}$ for local galaxies. The power-law index is fixed to 1/3, motivated by the assumption that there is a constant volume of gas available to be ionized, so that an increase in the total volume occupied by H II regions (as a result of an increase in the SFR) directly corresponds to a decrease in the volume occupied by the DIG (Oey et al. 2007). This assumption of density-bounded ionization is likely to be unphysical because the implied escape fraction of ionizing photons from local starburst galaxies would be much larger than what is observed (Oey et al. 2007). However, the functional form reproduces the general shape of the observed $\Sigma_{H\alpha}$ – $f_{H\alpha, \text{DIG}}$ trend.

Using Equation (6), we estimate $f_{H\alpha, \text{DIG}} \simeq 58\%$ at $z \sim 0$, $\sim 33\%$ at $z \sim 0.9$, $\sim 16\%$ at $z \sim 1.5$, and $\sim 0\%$ at $z \sim 2.2$. The decrease in the estimated DIG contribution with increasing redshift is consistent with the [S II]/ $H\alpha$ ratios measured from our stacked spectra, which decrease from 0.38 ± 0.01 at $z \sim 0$ to 0.19 ± 0.01 at $z \sim 2$ (see also Shapley et al. 2019).

3.4.3. Volume of the Star-forming Disk

The volume of the star-forming disk within R_e is computed assuming the disk is a cylinder with cross-sectional area πR_e^2 and height $2h_{\text{H II}}$, where $h_{\text{H II}}$ is the scale height of the star-forming disk. Ideally, $h_{\text{H II}}$ would be directly measured from $H\alpha$ observations of edge-on disk galaxies. However, $z \sim 0$ disk galaxies show strong extraplanar $H\alpha$ emission associated with DIG (e.g., Miller & Veilleux 2003; Rossa & Dettmar 2003; Bizyaev et al. 2017; Levy et al. 2019), meaning that the scale height of the star-forming disk cannot be measured from $H\alpha$ alone.

A reasonable alternative is to take the typical scale height of the molecular gas disk out of which the H II regions form and to correct this value upwards for the extra pressure support experienced by the ionized gas in the star-forming disk. The scale height and velocity dispersion of a thick and/or truncated gas disk are related by $h \simeq R_d \times \sigma_0 / v_{\text{rot}}$, where R_d is the disk

scale length, σ_0 is the intrinsic velocity dispersion and v_{rot} is the rotational velocity (e.g., Genzel et al. 2008). Assuming that H II regions and molecular clouds have similar radial distributions across galaxies, the kinematics and scale heights of the molecular and star-forming disks are related by

$$h_{\text{H II}} = h_{\text{mol}} \times (\sigma_0 / v_{\text{rot}})_{\text{H II}} / (\sigma_0 / v_{\text{rot}})_{\text{mol}}. \quad (7)$$

At fixed redshift, the typical velocity dispersion of ionized gas in SFGs is ~ 10 – 15 km s^{-1} larger than the average $\sigma_{0, \text{mol}}$ (Übler et al. 2019). The majority of this difference can be explained by the higher temperature of the ionized phase and the additional contribution of the H II region expansion to the measured velocity dispersion, which together are expected to contribute $\sim 15 \text{ km s}^{-1}$ in quadrature (e.g., Krumholz & Burkhardt 2016). Therefore, we assume that $\sigma_{0, \text{H II}} = (\sigma_{0, \text{mol}}^2 + 15^2)^{1/2}$.

Surveys of CO line emission in local spiral galaxies have found typical molecular gas velocity dispersions of ~ 12 – 13 km s^{-1} (Caldú-Primo et al. 2013; Levy et al. 2018). We adopt $\sigma_{0, \text{mol}} = 12.5 \text{ km s}^{-1}$, from which we estimate $\sigma_{0, \text{H II}} = 19.5 \text{ km s}^{-1}$. The ionized gas is expected to have a slightly lower v_{rot} than the molecular gas because of the extra pressure support (e.g., Burkert et al. 2010), but the percentage difference is observed to be small (e.g., Levy et al. 2018), so we assume that $v_{\text{rot, H II}} / v_{\text{rot, mol}} \simeq 1$. Molecular gas disks in the local universe have typical scale heights of 100–200 pc (e.g., Scoville et al. 1993; Pety et al. 2013; Kruijssen et al. 2019), so we adopt $h_{\text{mol}} = 150 \text{ pc}$. Combining all these numbers, we estimate $h_{\text{H II}} \simeq 230 \text{ pc}$.

At high z , the contribution of DIG to the $H\alpha$ emission is subdominant, but measurements of $H\alpha$ scale heights are very challenging due to surface brightness dimming. Elmegreen et al. (2017) measured an average rest-UV continuum scale height of $0.63 \pm 0.24 \text{ kpc}$ for galaxies at $z \sim 2$, suggesting that high- z disks are significantly thicker than their low- z counterparts. This is consistent with the elevated ionized gas velocity dispersions in high- z disks (e.g., Genzel et al. 2006, 2008; Wisnioski et al. 2015; Johnson et al. 2018; Übler et al. 2019).

We use measurements of R_d , v_{rot} , and σ_0 to estimate the median $h_{\text{H II}}$ at $z \sim 0.9$, 1.5, and 2.2. The $H\alpha$ flux profiles are assumed to be approximately exponential (motivated by studies of SFGs at similar redshifts; e.g., Nelson et al. 2013, 2016a; Wilman et al. 2020), which implies that $R_d = R_e / 1.67$. The v_{rot} and σ_0 values are measured by forward-modeling the one-dimensional velocity and velocity dispersion profiles extracted along the kinematic major axis of each galaxy, accounting for instrumental effects, beam smearing, and pressure support as described in Übler et al. (2019). Their sample of galaxies with reliable kinematic measurements includes 18/39 of the galaxies in our $z \sim 0.9$ stack, 13/36 galaxies in our $z \sim 1.5$ stack, and 16/65 galaxies in our $z \sim 2.2$ stack. We estimate $h_{\text{H II}}$ for each galaxy that is included in both our density sample and the Übler et al. (2019) kinematic sample and then calculate the median $h_{\text{H II}}$ for each redshift slice, yielding approximate ionized gas scale heights of 280 pc, 460 pc, and 540 pc at $z \sim 0.9$, 1.5, and 2.2, respectively. The $h_{\text{H II}}$ estimated for the $z \sim 2.2$ sample is consistent with the rest-UV continuum scale heights measured by Elmegreen et al. (2017) for galaxies at the same redshift.

3.4.4. Results

The calculated rms electron densities and volume filling factors are shown in Figure 5 and listed in Table 1. We give the values

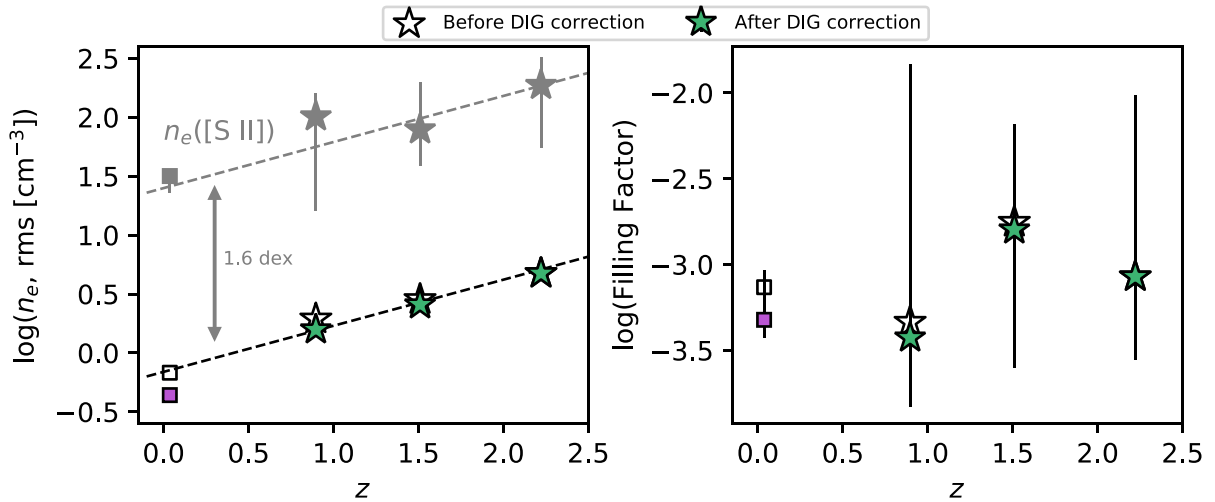


Figure 5. Redshift evolution of the rms electron density (left) and the volume filling factor of the line-emitting gas (right). Gray markers in the left-hand panel show the $n_e([\text{S II}])$ measurements for comparison. The plotting symbols are the same as in Figure 4. Open and colored solid markers indicate values before and after correcting for the contribution of DIG to the $\text{H}\alpha$ emission, respectively. Error bars are omitted from the open markers for clarity. The formal errors on the $n_e(\text{rms})$ measurements are too small to be seen. The two dashed lines in the left-hand panel were obtained by simultaneously fitting the redshift evolution of $n_e(\text{rms})$ and $n_e([\text{S II}])$, forcing both to have the same slope. The best-fit intercepts are offset by 1.6 dex.

Table 1

Thermal Pressure and Electron Density Calculated from the $[\text{S II}]$ Doublet Ratio, rms (Volume-averaged) Electron Density, and Volume Filling Factor of the Line-emitting Gas in Each of the Four Redshift Slices

Redshift Bin	$\log(P_{\text{th}}/k)([\text{S II}])$	$n_e([\text{S II}], \text{cm}^{-3})$	$n_e(\text{rms}, \text{cm}^{-3})$		$ff_{R_e} \times 10^3$	
			Original	DIG corrected	Original	DIG Corrected
$z \lesssim 0.1$	$5.78^{+0.01}_{-0.19}$	32^{+4}_{-9}	0.7 ± 0.1	0.4 ± 0.1	$0.7^{+0.7}_{-0.2}$	$0.5^{+0.4}_{-0.1}$
$z \sim 0.9$	$6.29^{+0.28}_{-0.73}$	101^{+59}_{-85}	1.9 ± 0.2	1.6 ± 0.1	$0.5^{+17.8}_{-0.3}$	$0.4^{+14.4}_{-0.2}$
$z \sim 1.5$	$6.23^{+0.43}_{-0.26}$	79^{+120}_{-40}	2.8 ± 0.3	2.6 ± 0.3	$1.8^{+5.6}_{-1.5}$	$1.6^{+5.0}_{-1.3}$
$z \sim 2.2$	$6.62^{+0.20}_{-0.53}$	187^{+140}_{-132}	4.7 ± 0.4	4.7 ± 0.4	$0.8^{+8.9}_{-0.6}$	$0.8^{+8.9}_{-0.6}$

Note. P/k is in units of K cm^{-3} . The $[\text{S II}]$ doublet ratio traces the local properties of the line-emitting gas. The rms electron density gives the average number of electrons per unit volume over the star-forming disk within R_e . We provide the values before and after correcting the $\text{H}\alpha$ luminosities for the contribution of diffuse ionized gas, as described in Section 3.4.2.

before and after correcting for the DIG contribution to indicate the magnitude of the correction, which is relatively small because $n_e(\text{rms})$ scales with $(1 - f_{\text{H}\alpha, \text{DIG}})^{1/2}$.²¹ The quoted errors on $n_e(\text{rms})$ indicate the standard error on the mean based on the $\text{H}\alpha$ flux uncertainties, but in reality, the error is dominated by the unknown systematic uncertainty on the line-emitting volume.

Figure 5 indicates that $n_e(\text{rms})$ evolves at a very similar rate to $n_e([\text{S II}])$, increasing by a factor of ~ 6 – 10 from $z \sim 0$ to $z \sim 2.2$. Consequently, our estimates suggest that there is no significant evolution of the volume filling factor over the probed redshift range. These conclusions hold independent of whether or not the DIG correction is applied.

The line-emitting volume is calculated assuming that $h_{\text{H II}}$ does not vary as a function of galactocentric radius. However, observations of constant ionized gas velocity dispersions across high- z disks (e.g., Genzel et al. 2006, 2011, 2017; Cresci et al. 2009) suggest that the scale height may grow exponentially with increasing galactocentric radius (e.g., Burkert et al. 2010). If we adopted a flared geometry the derived line-emitting volume would increase by a factor of 1.35. This would have a negligible impact on the derived rms electron densities (which scale with $h_{\text{H II}}^{-1/2}$) and

a minor impact on the derived filling factors (which scale with $h_{\text{H II}}^{-1}$). For the same reason, the relatively large uncertainties on the ionized gas scale heights have a limited impact on our results. A factor of 2 change in any or multiple of the adopted scale height values would not change the basic conclusion that $n_e(\text{rms})$ evolves much more rapidly than the ionized gas volume filling factor.

The consistency between the rate of evolution of $n_e([\text{S II}])$ and $n_e(\text{rms})$ seen in the left-hand panel of Figure 5 suggests that the filling factor of the line-emitting material inside H II regions may be approximately constant over cosmic time. This finding considerably reduces one major uncertainty in our understanding of the physical processes linking the evolution of $n_e([\text{S II}])$ to the evolution of galaxy properties.

The similarity between the redshift evolution of $n_e([\text{S II}])$ and $n_e(\text{rms})$ also provides further evidence to suggest that we are indeed observing a change in the density of the ionized material within H II regions over cosmic time. The $[\text{S II}]$ -emitting gas in a H II region with a radial n_e gradient will have a different n_e distribution depending on whether the nebula is ionization bounded or density bounded. Galaxies in the Local Group contain both ionization- and density-bounded H II regions (e.g., Pellegrini et al. 2012), and the elevated $[\text{O III}]/[\text{O II}]$ and $[\text{O III}]/\text{H}\beta$ ratios characteristic of high- z Ly α emitters could potentially be explained by density-bounded nebulae (e.g., Nakajima & Ouchi 2014). In a density-bounded nebula, the partially ionized zone is truncated,

²¹ We note that the rms density becomes lower after correcting for the DIG contribution, even though the DIG is less dense than the ionized gas in the H II regions, because there is no adjustment in the adopted line-emitting volume.

Table 2
[S II] λ 6716/[S II] λ 6731 Measurements for Stacks of KMOS^{3D}+ Galaxies in Bins below and above the Median in Various Galaxy Properties

Property	Median Value	Below Median	Above Median	Difference	Significance (σ)
		$R_{S\ II}$	$R_{S\ II}$		
$\Sigma_{SFR} (M_{\odot} \text{ yr}^{-1} \text{ kpc}^{-2})$	0.3	$1.38^{+0.06}_{-0.10}$	$1.16^{+0.09}_{-0.09}$	-0.22	1.6
$SFR (M_{\odot} \text{ yr}^{-1})$	23	$1.37^{+0.09}_{-0.07}$	$1.21^{+0.09}_{-0.12}$	-0.16	1.4
$\log(\Sigma_{\text{baryon}}/(M_{\odot} \text{ kpc}^{-2}))$	8.7	$1.39^{+0.07}_{-0.13}$	$1.17^{+0.11}_{-0.06}$	-0.22	1.3
$\log(\text{sSFR}/\text{yr}^{-1})$	-8.9	$1.39^{+0.04}_{-0.12}$	$1.17^{+0.14}_{-0.08}$	-0.21	1.2
$\log(\Sigma_{H_2}/(M_{\odot} \text{ kpc}^{-2}))$	8.4	$1.36^{+0.04}_{-0.13}$	$1.19^{+0.09}_{-0.08}$	-0.17	1.1
$\log(M_{H_2}/M_{*})$	0.06	$1.36^{+0.04}_{-0.11}$	$1.19^{+0.12}_{-0.09}$	-0.17	1.0
$\log(SFR/SFR_{MS(z)})$	0.0	$1.34^{+0.03}_{-0.16}$	$1.21^{+0.12}_{-0.05}$	-0.13	0.7
$\log(M_{*}/M_{\odot})$	10.2	$1.33^{+0.08}_{-0.09}$	$1.24^{+0.09}_{-0.10}$	-0.09	0.7
R_e (kpc)	3.4	$1.28^{+0.08}_{-0.08}$	$1.27^{+0.10}_{-0.09}$	-0.01	0.1

Note. Each bin contains 70 galaxies. The rows are sorted by decreasing significance of the difference between the [S II] ratios measured for the below- and above-median bins.

Table 3
Electron Densities and ISM Pressures Calculated from the $R_{S\ II}$ Measurements Presented in Table 2

Property	Below Median		Above Median		Difference		Significance (σ)	
	$\log(P_{th}/k)$	n_e (cm ⁻³)	$\log(P_{th}/k)$	n_e (cm ⁻³)	$\log(P_{th}/k)$	n_e (cm ⁻³)	$\log(P_{th}/k)$	n_e (cm ⁻³)
$\Sigma_{SFR} (M_{\odot} \text{ yr}^{-1} \text{ kpc}^{-2})$	$6.03^{+0.46}_{-1.25}$	44^{+86}_{-41}	$6.73^{+0.19}_{-0.20}$	257^{+138}_{-109}	0.70	213	1.4	1.5
$SFR (M_{\odot} \text{ yr}^{-1})$	$6.09^{+0.33}_{-2.09}$	52^{+64}_{-51}	$6.62^{+0.25}_{-0.27}$	193^{+170}_{-82}	0.54	141	1.3	1.4
$\log(\Sigma_{\text{baryon}}/(M_{\odot} \text{ kpc}^{-2}))$	$5.96^{+0.59}_{-1.96}$	38^{+108}_{-37}	$6.72^{+0.13}_{-0.28}$	252^{+98}_{-121}	0.76	214	1.2	1.3
$\log(\text{sSFR}/\text{yr}^{-1})$	$5.94^{+0.57}_{-0.52}$	39^{+99}_{-27}	$6.73^{+0.17}_{-0.41}$	246^{+125}_{-141}	0.79	207	1.1	1.2
$\log(\Sigma_{H_2}/(M_{\odot} \text{ kpc}^{-2}))$	$6.13^{+0.48}_{-0.35}$	58^{+115}_{-29}	$6.65^{+0.17}_{-0.26}$	214^{+125}_{-91}	0.52	156	1.0	1.1
$\log(M_{H_2}/M_{*})$	$6.09^{+0.46}_{-0.29}$	55^{+99}_{-22}	$6.68^{+0.20}_{-0.37}$	216^{+143}_{-113}	0.59	161	1.0	1.1
$\log(SFR/SFR_{MS(z)})$	$6.19^{+0.52}_{-0.14}$	72^{+159}_{-23}	$6.63^{+0.10}_{-0.42}$	192^{+63}_{-109}	0.44	120	0.7	0.6
$\log(M_{*}/M_{\odot})$	$6.26^{+0.34}_{-0.56}$	85^{+81}_{-62}	$6.55^{+0.22}_{-0.31}$	160^{+130}_{-70}	0.28	75	0.6	0.7
R_e (kpc)	$6.46^{+0.20}_{-0.38}$	128^{+81}_{-73}	$6.51^{+0.20}_{-0.43}$	139^{+100}_{-84}	0.05	11	0.1	0.1

meaning that the observed [S II] emission would originate from material at smaller radii, which could have a higher average n_e compared to the ionization-bounded case. It is therefore hypothetically possible that some or all of the measured n_e ([S II]) evolution could be driven by a decrease in the fraction of ionization-bounded regions with increasing redshift, rather than by a change in the average gas conditions within H II regions. However, the strong evolution of n_e (rms) suggests that changing gas conditions are the dominant source of the observed n_e ([S II]) evolution.

4. Trends between Electron Density and Galaxy Properties

We begin our investigation into the physical origin of the density evolution by exploring how the electron density varies as a function of various galaxy properties, first within the KMOS^{3D}+ sample (Section 4.1) and then using the extended data set (Section 4.2).

4.1. Trends in Electron Density within KMOS^{3D}+

We explore which galaxy properties are most closely linked to the density variation within the KMOS^{3D}+ sample by dividing the galaxies into two bins (below and above the median) in various star formation, gas, and structural properties: M_{*} , SFR, sSFR, Σ_{SFR} , offset from the star-forming MS ($SFR/SFR_{MS(z)}$), molecular gas fraction μ_{H_2} ($=M_{H_2}/M_{*}$), molecular gas mass surface density Σ_{H_2} , baryonic surface density Σ_{baryon} , and R_e . The molecular gas properties are estimated by assuming that the galaxies lie along the

Tacconi et al. (2020) scaling relation for the molecular gas depletion time t_{depl} as a function of z , offset from the star-forming MS and M_{*} . The derived t_{depl} is multiplied by SFR to obtain the molecular gas mass M_{H_2} . Σ_{SFR} is defined as $SFR/(2\pi R_e^2)$, and similar definitions apply to all other surface density quantities. The calculated surface densities represent the conditions in the central regions of the galaxies.

Σ_{baryon} is defined as the total surface density of the stellar, molecular gas, and atomic gas components. We adopt a constant atomic gas mass surface density of $\Sigma_{\text{HI}} = 6.9 M_{\odot} \text{ pc}^{-2}$ based on the tight observed relationship between the masses and diameters of HI disks in the local universe (Broeils & Rhee 1997; Wang et al. 2016). The gas reservoirs in the star-forming disks of high- z SFGs are expected to be dominated by H_2 (Tacconi et al. 2018, 2020, and references therein), and therefore the assumption of a redshift-invariant Σ_{HI} is unlikely to have any significant impact on the baryonic surface densities derived for the KMOS^{3D}+ galaxies (see discussion in Appendix C).

We stack the spectra of the galaxies below and above the median in each property, and measure $R_{S\ II}$, n_e ([S II]) and $\log(P_{th}/k)$ ([S II]) for each stack. Table 2 lists the median value of each galaxy property, the [S II] ratios measured for the below-median and above-median stacks, the differences between the [S II] ratios measured for the below- and above-median stacks, and the statistical significance of these differences. We note that the median values are calculated for each property individually and, therefore, the combination of these parameters does not necessarily represent a ‘‘typical’’ galaxy. Table 3 lists the n_e ([S II]) and

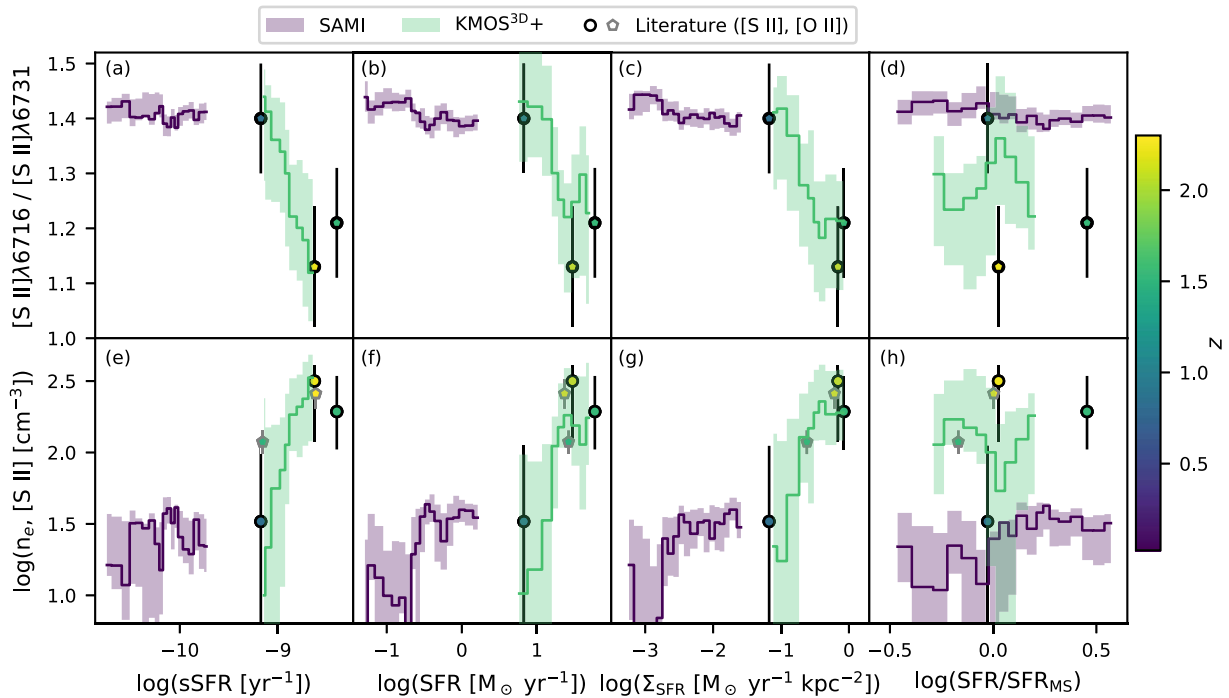


Figure 6. [S II] ratio (top) and n_e ([S II]) (bottom) as a function of sSFR ((a) and (e)), SFR ((b) and (f)), Σ_{SFR} ((c) and (g)), and $\text{SFR}/\text{SFR}_{\text{MS}(z)}$ ((d) and (h)). The solid lines and shaded error regions represent the average properties of the SAMI (purple) and KMOS^{3D+} (green) galaxies, computed in sliding bins as described in Section 4.2. The individual data points are measurements for literature samples of high- z SFGs, introduced in Section 3.3. In the bottom panel, n_e ([O II]) measurements (points with gray outlines) have been included to illustrate the consistency between measurements made using different tracers. The color-coding indicates the median redshift of each galaxy sample.

$\log(P_{\text{th}}/k)$ ([S II]) values calculated from the [S II] ratios listed in Table 2, as well as the differences and statistical significance of the differences between the values measured for the below- and above-median stacks.

We find the most significant differences between the [S II] ratios of galaxies below and above the median in Σ_{SFR} , SFR, Σ_{baryon} , and sSFR. The galaxies with comparably weak star formation and/or low Σ_{baryon} have electron densities and ISM pressures similar to those of local star-forming galaxies, whereas the galaxies with strong star formation and/or high Σ_{baryon} have densities and pressures that are comparable to or exceed the typical values for $z \sim 2$ SFGs (see Figure 3). $R_{\text{S II}}$ is also mildly anticorrelated with Σ_{H_2} and μ_{H_2} . There is a weak trend toward lower $R_{\text{S II}}$ at higher $\text{SFR}/\text{SFR}_{\text{MS}(z)}$ and M_* , the latter of which is likely driven by the positive correlation between M_* and SFR. Our results are consistent with previous findings that the electron density is positively correlated with the level of star formation in galaxies (e.g., Shimakawa et al. 2015; Kaasinen et al. 2017; Jiang et al. 2019; Kashino & Inoue 2019). However, the trend with Σ_{baryon} suggests that the weight of the stars and ISM may also influence the density of the ionized gas in H II regions.

Within the KMOS^{3D+} sample, there is no evidence that the density is correlated with R_e , suggesting that the n_e ([S II]) evolution is unlikely to be explained solely by the size evolution of galaxies.

4.2. Trends in Electron Density across $0 \lesssim z \lesssim 2.6$

We use the extended data set to investigate the relationship between electron density and global galaxy properties over a much larger dynamic range. Figure 6 shows how $R_{\text{S II}}$ (top) and n_e ([S II]) (bottom) vary as a function of sSFR, SFR, Σ_{SFR} , and $\text{SFR}/\text{SFR}_{\text{MS}(z)}$. The galaxy samples are color-coded by median redshift.

We explore the trends within the SAMI and KMOS^{3D+} samples by measuring the [S II] ratio in sliding bins. For the KMOS^{3D+} sample, we sort the galaxies by the quantity on the x -axis (e.g., sSFR), stack the first 50 galaxies, and calculate $R_{\text{S II}}$ and n_e . The bin boundary is then moved across by 10 galaxies, and the stacking is repeated for galaxies number 10–60, followed by galaxies number 20–70, etc., resulting in a total of nine bins. We perform measurements in sliding bins because it minimizes biases associated with the arbitrary choice of bin boundaries and gives a much clearer picture of the overall trends. However, the sliding bin measurements are highly correlated and are therefore not used in any quantitative analysis.

The same procedure is applied to the SAMI galaxies, except that we stack in bins of 100 galaxies and move the bin boundary by 20 galaxies at a time, resulting in a total of 18 bins. The larger bin size is chosen to mitigate the effects of line-ratio fluctuations in the low-density limit. At the typical densities of the SAMI galaxies, $R_{\text{S II}}$ changes very slowly as a function of n_e (see left-hand panel of Figure 4). Small line-ratio fluctuations can lead to disproportionately large density fluctuations, which are partially smoothed out by the larger bins.

We find that the electron density is positively correlated with sSFR, SFR, and Σ_{SFR} , in good agreement with previous results (e.g., Shimakawa et al. 2015; Herrera-Camus et al. 2016; Kashino & Inoue 2019). The trends among the high- z samples appear to be much steeper than the trends within the SAMI sample, but it is unclear whether this reflects an intrinsic difference in the relationship between n_e and the level of star formation at different cosmic epochs, or whether it is an artifact of the flattening of the n_e - $R_{\text{S II}}$ relationship at $n_e \lesssim 40 \text{ cm}^{-3}$.

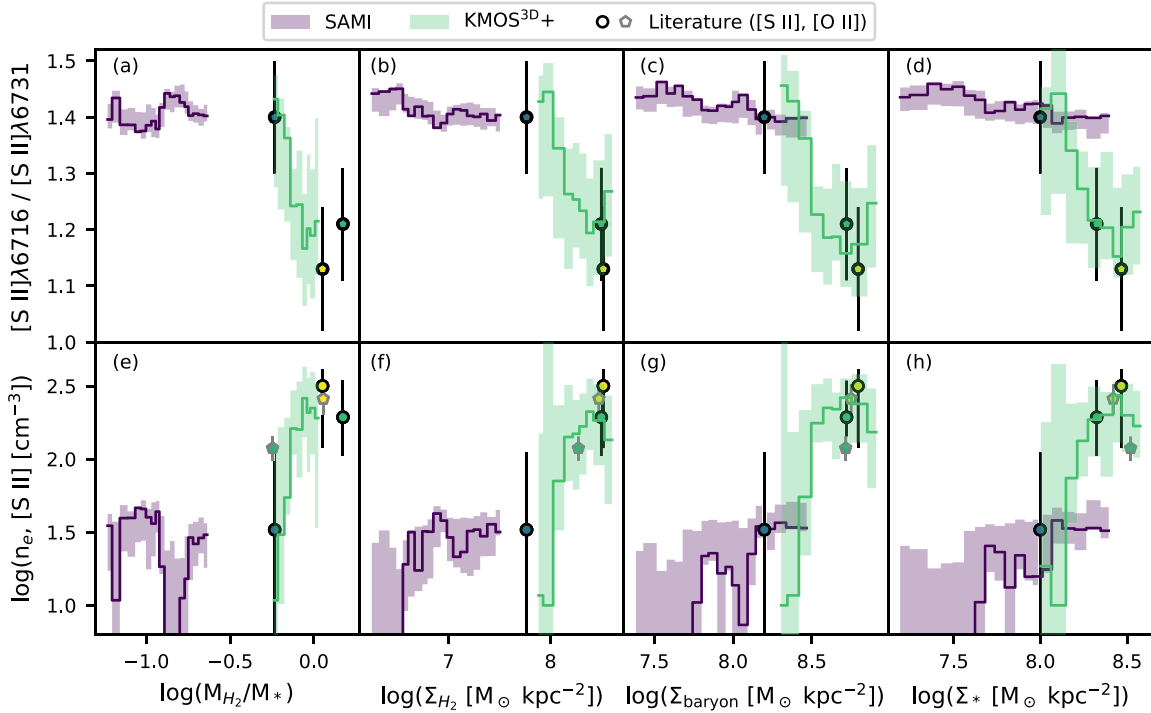


Figure 7. [S II] ratio (top) and n_e ([S II]) (bottom) as a function of μ_{H_2} ((a) and (e)), Σ_{H_2} ((b) and (f)), Σ_{baryon} ((c) and (g)), and Σ_* ((d) and (h)). The color-coding, symbols, and data representation are the same as in Figure 6.

From Figure 6, it appears that the electron density is not intrinsically related to offset from the star-forming MS. The KMOS^{3D+} galaxies have systematically higher n_e ([S II]) (lower $R_{\text{S II}}$) than the SAMI galaxies at a fixed MS offset. This, combined with the overall roughly monotonic variations in $R_{\text{S II}}$ and n_e as a function of SFR, sSFR, and Σ_{SFR} (see also Kaasinen et al. 2017), suggests that the redshift evolution of the electron density is likely to be linked to the evolving normalization of the star-forming MS.

Figure 7 shows $R_{\text{S II}}$ (top) and n_e ([S II]) (bottom) vary as a function of μ_{H_2} , Σ_{H_2} , Σ_{baryon} , and Σ_* . μ_{H_2} is directly related to sSFR through the molecular gas depletion time and, therefore, the two quantities show very similar trends with n_e . The same is true for Σ_{H_2} and Σ_{SFR} . Our data are consistent with a single positive correlation between Σ_{baryon} and n_e across $0 \lesssim z \lesssim 2.6$, but the KMOS^{3D+} galaxies are clearly offset to higher n_e ([S II]) than the SAMI galaxies at fixed Σ_* . This supports our earlier hypothesis that any correlation between n_e and M_* is primarily driven by the M_* -SFR relation and provides further evidence to suggest that the evolving gas content of galaxies—which drives the evolution of the normalization of the star-forming MS—may also be an important driver of the n_e evolution.

5. What Drives the Redshift Evolution of Galaxy Electron Densities?

We use our measurements to investigate possible physical driver(s) of the evolution of the electron density and thermal pressure across $0 \lesssim z \lesssim 2.6$. We focus on four scenarios that are commonly discussed in the literature: that the electron density is governed by (1) the density of the parent molecular cloud (Section 5.1), (2) the pressure injected by stellar feedback (Section 5.2), (3) the pressure of the ambient medium (Section 5.3), or (4) the dynamical evolution of the H II region

(Section 5.4). In this analysis, we explicitly account for the average properties of the galaxies in each stack, meaning that the presented interpretation does not rely on the assumption that our samples are representative of the underlying SFG population at each redshift, or that the samples probe the same subset of the galaxy population at each redshift.

5.1. Scenario 1: H II Region Density and Thermal Pressure Governed by Molecular Cloud Density

Stars form in the centers of molecular clouds and radiate high-energy photons that dissociate and ionize the surrounding ISM material to form H II regions. Therefore, the initial electron densities of H II regions are likely to be set by the molecular hydrogen number density. Because each H_2 molecule contributes two electrons, $n_e \simeq 2 n_{\text{H}_2}$.

The mass volume density of molecular hydrogen (ρ_{H_2}) within R_e is derived by dividing Σ_{H_2} by the molecular gas scale height h_{mol} , which is estimated using the procedures described in Section 3.4.3. We adopt $h_{\text{mol}} = 150$ pc at $z \sim 0$ and estimate the median h_{mol} at $z \sim 0.9$, 1.5, and 2.2 assuming $h_{\text{mol}} \simeq R_d \times \sigma_{0,\text{mol}}/v_{\text{rot,mol}}$. The molecular gas kinematics are estimated from the measured ionized gas kinematics accounting for the expected difference in the pressure support experienced by the two gas phases (e.g., Burkert et al. 2010). These calculations yield typical molecular gas scale heights of ~ 180 pc, ~ 420 pc, and ~ 490 pc at $z \sim 0.9$, 1.5, and 2.2, respectively.

We divide ρ_{H_2} by the molecular mass of H_2 to obtain n_{H_2} . Column (a) of Figure 8 compares the evolution of n_{H_2} to the evolution of n_e ([S II]) (top), $\log(P_{\text{th}}/k)$ ([S II]) (middle), and n_e (rms) (bottom). The blue and red dashed lines are the best fits obtained when the slope is (i) fixed to unity and (ii) left free, respectively. The shaded regions indicate the 1σ errors around the best fits, obtained by randomly perturbing each data point

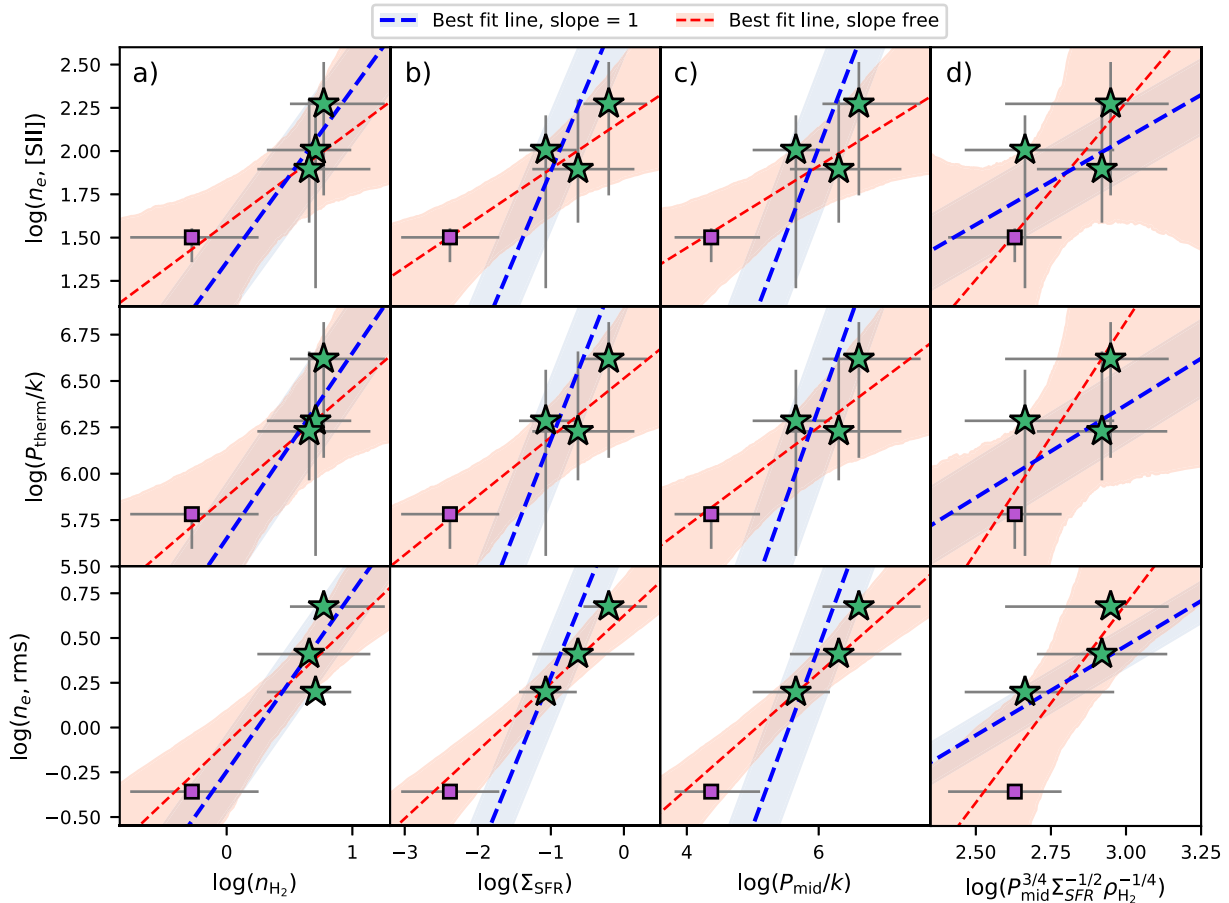


Figure 8. Relationships between the thermal properties of the ionized gas—probed by (top) n_e [S II], (middle) $\log(P_{\text{th}}/k)$ [S II], and (bottom) n_e (rms)—and selected galaxy properties: (a) n_{H_2} , (b) Σ_{SFR} , (c) midplane pressure P_{mid} , and (d) $\Sigma_{\text{SFR}}^{-1/2} \rho_{\text{H}_2}^{-1/4} P_{\text{mid}}^{3/4}$, which is proportional to the inverse of the predicted H II region stall radius. The n_e (rms) measurements have been corrected for DIG contamination as described in Section 3.4.2. Plotting symbols are the same as in Figure 4. Error bars on the x-axis quantities indicate the 16th–84th percentile range in galaxy properties within each stack. The blue and red dashed lines are the best fits obtained when the slope is (i) fixed to unity and (ii) left free, respectively. The shaded regions show the 1σ errors around the best fits, obtained by randomly perturbing each data point according to its errors and refitting 1000 times. When the blue and red lines match, the quantities on the x- and y-axes are consistent with having a 1:1 relationship (in log space) at all redshifts.

according to its errors and refitting 1000 times, and then computing the 16th–84th percentile range of these 1000 fits. A good match between the red and blue lines indicates that the quantities on the x- and y-axes are consistent with having a 1:1 relationship (in log space) at all redshifts. Any significant inconsistency between the blue and red lines in Column (a) would suggest that the relationship between n_e and n_{H_2} changes over cosmic time, meaning that additional physical processes would need to be considered in order to explain the n_e evolution.

The blue and red lines in Column (a) are very consistent with one another, indicating that there is an approximately linear relationship between n_e (rms) and n_{H_2} . The mean n_e (rms)/ n_{H_2} ratio across the four redshift slices is ~ 0.6 . This relationship is averaged over the assumed volumes of the star-forming and molecular disks, and to obtain the average coefficient for individual star-forming regions, one would need to multiply by the ratio of the volume filling factor of molecular clouds within $2\pi R_e^2 h_{\text{mol}}$ to the volume filling factor of H II regions within $2\pi R_e^2 h_{\text{H II}}$. The discrepancy between the estimated coefficient of 0.6 and the predicted coefficient of 2 could very likely be accounted for by the systematic uncertainties introduced by the various assumptions made in our calculations. Therefore, we

suggest that the elevated electron densities in H II regions at high z could plausibly be the direct result of larger molecular hydrogen densities in the parent molecular clouds.

5.2. Scenario 2: H II Region Density and Thermal Pressure Governed by Stellar Feedback

Although H II regions are expected to form with $n_e \simeq 2 n_{\text{H}_2}$, the electron density may change over time as a result of energy injection and/or H II region expansion. It has been suggested that the strong correlation between n_e and the level of star formation in galaxies may arise because stellar feedback injects energy into H II regions, increasing the internal pressure and electron density (e.g., Groves et al. 2008; Krumholz & Matzner 2009; Kaasinen et al. 2017; Jiang et al. 2019).

The turbulent pressure injected by stellar feedback can be parameterized as $P_{\text{inj}} = \Sigma_{\text{SFR}} (p_*/m_*)/4$, where p_*/m_* is the amount of momentum injected into the ISM per solar mass of star formation, and the factor of 1/4 represents the fraction of the total momentum in the vertical component on one side of the disk (Ostriker & Shetty 2011; Kim et al. 2013). The value of p_*/m_* scales with the number of supernovae per solar mass of star formation and is therefore strongly dependent on the initial mass function. ISM simulations have not yet reached a

consensus on the amount of momentum injected per supernova explosion. It has been suggested that the momentum injection may be sensitive to small-scale properties such as the spatial clustering of supernovae (e.g., Gentry et al. 2019) and the interaction between the hot ejecta and the surrounding ISM (e.g., Kim & Ostriker 2015), but differences in numerical methods lead to large discrepancies between different simulation results. Sun et al. (2020) find a linear correlation between Σ_{SFR} and the turbulent pressure of molecular clouds in local spiral galaxies, suggesting that p_*/m_* is approximately constant. We assume that p_*/m_* is constant and independent of redshift, meaning that $P_{\text{inj}} \propto \Sigma_{\text{SFR}}$. In other words, we can investigate the link between n_e and pressure injection by stellar feedback without needing to assume a specific value for p_*/m_* .

Column (b) of Figure 8 indicates that the relationship between electron density and Σ_{SFR} is likely to be significantly flatter than linear. This suggests that the increase in the rate of turbulent pressure injection toward higher redshifts does not directly lead to the observed increase in n_e . The sublinearity of the relationship could potentially indicate that the fraction of injected pressure that is confined within H II regions decreases toward higher redshifts. In order for the data to be consistent with a linear relationship between n_e and the confined pressure, the fraction of pressure leaking out of H II regions would have to increase by an order of magnitude from $z \sim 0$ to $z \sim 2.2$. The increased incidence of outflows at high z (e.g., Steidel et al. 2010; Newman et al. 2012; Förster Schreiber et al. 2019) could lead to a significant reduction in the pressure confinement efficiency, although our explicit removal of objects with detected galaxy-scale outflows limits the possible magnitude of such an effect in our data set.

Alternatively, the relationship between n_e and the confined feedback pressure could be intrinsically sublinear, perhaps because (a) the fraction of the injected turbulent pressure that cascades into the thermal pressure of the 10^4 K gas decreases steeply with increasing Σ_{SFR} and/or z , (b) n_e is *not* governed by the internal H II region pressure, or (c) n_e is governed by the internal pressure, but stellar feedback is not the primary source of internal pressure across some or all of the parameter space covered by our sample. The total pressure within a H II region is the sum of many components including the turbulent and thermal pressure of the 10^4 K gas, the hot gas pressure associated with supernova ejecta and shocked stellar winds, and radiation pressure (e.g., Krumholz & Matzner 2009; Murray et al. 2010). Quantitative predictions for the relationship between n_e and P_{inj} from multiphase simulations of H II regions including outflows and all major pressure components (e.g., Rahner et al. 2017, 2019), as well as more complete observational censuses of the relative contributions of different pressure components within H II regions (e.g., Lopez et al. 2014; McLeod et al. 2019, 2020), would assist to determine which of these scenarios is most likely.

5.3. Scenario 3: H II Region Density and Thermal Pressure Governed by the Ambient Pressure

H II regions form by dissociating and ionizing molecular gas and are therefore initially overpressured with respect to their surroundings. They expand toward lower pressures and densities until they reach equilibrium with the ambient medium. Analytic models suggest that in populations of H II regions with average ages $\gtrsim 1$ Myr, the majority should be

close to their equilibrium sizes and pressures (e.g., Oey & Clarke 1997; Nath et al. 2020).

The relationship between $n_e(\text{rms})$, $n_e([\text{S II}])$, and the pressure of the external ambient medium depends on the balance between the different internal pressure components. There is some observational evidence to suggest that in local H II regions, $n_e(\text{rms})$ scales linearly with the disk midplane pressure. Elmegreen & Hunter (2000) noted that the volume-averaged thermal pressures of the largest H II regions in nearby massive spiral galaxies are comparable to the average disk midplane pressures (assuming $T_e = 10^4$ K). Gutiérrez & Beckman (2010) measured $n_e(\text{rms})$ for individual H II regions in a spiral galaxy and a dwarf irregular galaxy and found that in both galaxies, the electron density declines exponentially with a scale length similar to that of the H I column density profile. The roughly linear relationship between $n_e(\text{rms})$ and the ambient pressure suggests that the thermal pressure of the 10^4 K gas must account for an approximately constant fraction of the total H II region pressure.

If the majority of H II regions at $0 \leq z \leq 2.6$ are in pressure equilibrium with their surroundings, and the balance between the different internal pressure components does not change significantly over time, then $n_e(\text{rms}) \times T_e$ should evolve at approximately the same rate as the midplane pressure. We do not expect the average T_e to vary significantly between our four redshift slices because we measure similar gas-phase metallicities from all four stacks (the increase in median stellar mass toward higher redshift offsets the evolution of the mass-metallicity relation). Therefore, we estimate the average midplane pressure within R_e at each redshift and test whether the midplane pressure evolves at a similar rate to n_e .

The pressure at the midplane of a disk in hydrostatic equilibrium is given by

$$P_{\text{mid}} \simeq \frac{\pi G}{2} \Sigma_{\text{H I}+\text{H}_2} \left(\Sigma_{\text{H I}+\text{H}_2} + \frac{\sigma_g}{\sigma_*} \Sigma_* \right), \quad (8)$$

where Σ_* is the stellar mass surface density, $\Sigma_{\text{H I}+\text{H}_2}$ is the atomic + molecular gas mass surface density, σ_g is the velocity dispersion of the neutral gas (which we assume to be given by $\sigma_{0,\text{mol}}$), and σ_* is the stellar velocity dispersion (Elmegreen 1989). The stellar velocity dispersion is estimated from Σ_* assuming hydrostatic equilibrium, as outlined in Appendix D.

Column (c) of Figure 8 compares the evolution of P_{mid} to the evolution of the electron density and thermal pressure. Again, we find that the best-fit relationships have slopes significantly below unity, suggesting that the thermal pressure of the 10^4 K gas accounts for a decreasing fraction of the total H II region pressure with increasing redshift.

The implied change in the H II region internal pressure balance can be understood by considering the sources of the different pressure components. The electron density increases by a factor of ~ 6 – 10 from $z \sim 0$ to $z \sim 2.2$, which drives a similar change in the thermal pressure of the 10^4 K gas. The ratio of turbulent to thermal pressure in the 10^4 K gas is given by $\sigma_{0,\text{ion}}^2/c_s^2$. The sound speed c_s scales with $T_e^{1/2}$ and is therefore not expected to vary significantly with redshift, but $\sigma_{0,\text{ion}}^2$ increases by a factor of ~ 4 from $z \sim 0$ to $z \sim 2.2$ (e.g., Genzel et al. 2006; Wisnioski et al. 2015; Johnson et al. 2018; Übler et al. 2019), driven by gravitational instabilities in marginally stable gas-rich disks (e.g., Krumholz et al. 2018; Übler et al. 2019). The radiation pressure

and hot gas pressure both scale almost linearly with the average SFR (e.g., Oey & Clarke 1997; Murray et al. 2010; Ostriker & Shetty 2011), which is approximately two orders of magnitude larger for a $\log(M_*/M_\odot) = 10.3$ galaxy at $z \sim 2.2$ than for a $\log(M_*/M_\odot) = 9.6$ galaxy at $z \sim 0$. Therefore, the ratio of the thermal pressure of the 10^4 K gas to the total H II region pressure could easily change by at least an order of magnitude over the probed redshift range.

We conclude that n_e could plausibly be set by the interplay between the external ambient pressure and the internal pressure balance, but not by the ambient pressure alone.

5.4. Scenario 4: H II Region Density and Thermal Pressure Governed by Dynamical Evolution

There is an inverse linear correlation between the diameter and $n_e(\text{rms})$ of local H II regions (e.g., Kim & Koo 2001; Dopita et al. 2006; Hunt & Hirashita 2009), suggesting that the dynamical evolution of H II regions may play an important role in regulating their electron densities. Oey & Clarke (1997, 1998) presented an analytic model for the size evolution of a H II region assuming that the internal pressure is dominated by shocked stellar winds and supernova ejecta. They postulated that the H II region will expand as an energy-driven bubble until the internal pressure is comparable to the ambient pressure, at which point the H II region “stalls”. The stall radius scales as $R_{\text{stall}} \propto \Sigma_{\text{SFR}}^{1/2} \rho_{\text{H}_2}^{1/4} P_{\text{mid}}^{-3/4}$ (see derivation in Appendix E). The final size of the H II region is determined by the balance between the combined mechanical luminosity of the central star cluster and the internal gas pressure, which both drive the expansion of the H II region, and the ambient pressure which resists the expansion.

Oey & Clarke (1997) used their model to predict the slope of the H II region size distribution and showed that the majority of H II regions are expected to be close to their maximum sizes. The predicted size distribution is consistent with the observed size distribution of H I holes in local spiral galaxies (Oey & Clarke 1997; Bagetakos et al. 2011). If the majority of H II regions at $0 \leq z \leq 2.6$ have sizes close to the stall radii predicted by Oey & Clarke (1997), and the size- $n_e(\text{rms})$ correlation observed in the local universe extends to higher redshifts, then we might expect to observe an inverse linear correlation between $n_e(\text{rms})$ and R_{stall} , or equivalently, a (positive) linear correlation between $n_e(\text{rms})$ and $\Sigma_{\text{SFR}}^{-1/2} \rho_{\text{H}_2}^{-1/4} P_{\text{mid}}^{3/4}$.

We investigate whether or not such a correlation exists in Column (d) of Figure 8. The relationship between $\Sigma_{\text{SFR}}^{-1/2} \rho_{\text{H}_2}^{-1/4} P_{\text{mid}}^{3/4}$ and $n_e(\text{rms})$ appears to be slightly super-linear, but the correlation between $\Sigma_{\text{SFR}}^{-1/2} \rho_{\text{H}_2}^{-1/4} P_{\text{mid}}^{3/4}$ and $n_e([\text{S II}])$ is approximately linear and could potentially be consistent with an inverse linear relationship between n_e and R_{stall} . This suggests that the elevated electron densities in high- z SFGs could plausibly be driven by a decrease in the ratio of the injected hot gas pressure (which drives H II region expansion) to the midplane pressure (which resists the expansion).

However, we note that the adopted expression for the stall radius is based on a few simplifying assumptions which may not reflect the conditions in H II regions at high z . The most basic assumption is that each star cluster ionizes a spherical H II region that does not overlap with regions ionized by adjacent clusters. Extreme star-forming regions in the local universe often show more complex geometries, with neighboring star clusters ionizing overlapping areas within a single giant

molecular cloud (e.g., Förster Schreiber et al. 2001; Snijders et al. 2007). If these conglomerations of H II regions reflect the typical conditions in rapidly star-forming galaxies at high z , the stall radius may indicate the typical extent of the ionized region associated with an individual star cluster, rather than a characteristic spherical H II region size.

The second key assumption is that the H II region expansion is primarily driven by mechanical energy from stellar winds and supernovae. These processes produce highly pressurized hot gas, which, if confined, can efficiently drive the expansion of a H II region (e.g., Castor et al. 1975). However, observations of Milky Way H II regions indicate that the pressure in the hot gas is comparable to the pressure in the 10^4 K gas (e.g., McKee et al. 1984; Dorland & Montmerle 1987; Harper-Clark & Murray 2009), suggesting that much of the hot gas may escape through holes in the expanding bubbles (e.g., Murray et al. 2010). If the hot gas pressure is significantly lower than predicted, the dynamics of H II regions may be governed by other forms of pressure, such as the thermal pressure of the 10^4 K gas (e.g., Spitzer 1978; Dyson & Williams 1980) or radiation pressure. Photons trapped in the expanding shell of a H II region will provide an extra source of acceleration, increasing the expansion velocity of the shell and the final stall radius. Radiation is predicted to govern the dynamics of H II regions around luminous massive clusters (e.g., Krumholz & Matzner 2009; Murray et al. 2010) and may therefore be significant at high z . However, thermal pressure and mechanical feedback are observed to be dominant in more typical local H II regions (e.g., Lopez et al. 2014; McLeod et al. 2019, 2020).

It is unclear how the relationship between n_e and R_{stall} would change if a different expansion mechanism was considered. Stall radius expressions have been derived for thermal-pressure-driven expansion assuming that the expansion stalls when thermal pressure equilibrium is achieved (Dyson & Williams 1980) and for radiation-pressure-driven expansion assuming that the expansion stalls when the expansion velocity becomes comparable to the velocity dispersion in the parent cloud (Krumholz & Matzner 2009). An investigation of how these stall conditions relate to the total pressure equilibrium condition for different ratios of thermal to total pressure is beyond the scope of this paper. Simulations of H II region evolution including all major internal pressure components as well as varying fractions of turbulent pressure in the ambient medium (such as those presented in Rahner et al. 2017, 2019) will help to better understand how the dynamical evolution and stall radii of H II regions vary as a function of the luminosity and evolutionary stage of the cluster and the properties of the surrounding medium.

5.5. Implications

In this section, we have compared the observed n_e evolution to quantitative predictions for four potential drivers of the density evolution. We found that $n_e \simeq n_{\text{H}_2}$, suggesting that the elevated electron densities in H II regions at high- z could plausibly be the direct result of higher gas densities in the parent molecular clouds. We investigated whether the strong relationship between n_e and the level of star formation in galaxies could arise because n_e is governed by pressure injection from stellar feedback. Our data suggest that the increase in the amount of turbulent pressure injected by stellar winds and supernovae toward higher redshifts does not directly

lead to the observed increase in n_e . Further constraints from observations and simulations are required to determine which additional parameters control the relationship between these two quantities.

We explored whether the n_e evolution could be driven by a change in the equilibrium internal pressure of H II regions. We found that the ambient pressure evolves much faster than n_e , suggesting that n_e could be governed by the interplay between the ambient pressure and the balance between different sources of pressure within H II regions, but not by the ambient pressure alone. Finally, motivated by the existence of a strong inverse correlation between n_e (rms) and H II region size in the local universe, we investigated whether the n_e evolution could be linked to a change in the balance between the energy injection from stellar feedback (which drives H II region expansion) and the ambient pressure (which resists the expansion). We found tentative evidence for an inverse linear correlation between n_e and the H II region stall radius R_{stall} , but noted that the functional form of R_{stall} relies on some assumptions that may not hold at high z .

The evolution of R_{stall} is governed by the balance between the increases in Σ_{SFR} and ρ_{H_2} (which lead to larger R_{stall}) and the increase in P_{mid} (which leads to smaller R_{stall}). The fact that the predicted R_{stall} decreases with increasing redshift indicates that the P_{mid} term is dominant. Of the terms that contribute to P_{mid} , the typical values of Σ_{HI} and σ_g/σ_* do not vary significantly across the redshift range probed by our samples, whereas the median Σ_* in our $z \sim 2.2$ sample is ~ 0.7 dex higher than the median Σ_* in our $z \sim 0$ sample, and the median Σ_{H_2} is 1.5 dex higher in our $z \sim 2.2$ sample than in our $z \sim 0$ sample. Therefore, the increase in P_{mid} is primarily driven by the increase in Σ_{H_2} .

We conclude that, in the plausible scenario where the electron density is governed by either n_{H_2} or $1/R_{\text{stall}}$, the increase in electron density from $z \sim 0$ to $z \sim 2.6$ would be primarily driven by the increase in the molecular gas fractions of galaxies. This is consistent with our earlier hypothesis that the n_e evolution is linked to the evolving normalization of the star-forming MS (Section 4.2), which is also driven by the evolution of galaxy molecular gas reservoirs (e.g., Tacconi et al. 2020).

Finally, we note that the three rows of panels in Figure 8 indicate that n_e ([S II]), $\log(P_{\text{th}}/k)$ ([S II]), and n_e (rms) evolve at very similar rates. The thermal pressure is expected to be approximately constant within any given H II region and is therefore likely to be a more meaningful description of the gas conditions than n_e which can show strong radial gradients (see, e.g., Kewley et al. 2019 and references therein). However, the conclusions presented in this section are not strongly dependent on which of the three quantities is considered.

6. Conclusions

We have investigated the evolution of the typical electron density in SFGs from $z \sim 2.6$ to $z \sim 0$, using a sample of 140 galaxies at $0.6 < z < 2.6$ drawn primarily from the KMOS^{3D} survey and a sample of 471 galaxies at $z \sim 0$ from the SAMI Galaxy Survey. The KMOS^{3D} sample is distributed in three redshift bins ($z \sim 0.9$, 1.5, and 2.2) and allows us to analyze the density evolution over ~ 5 Gyr of cosmic history with a single data set. We select galaxies that do not show evidence of AGN activity or broad-line emission indicative of outflows in order to minimize contamination from line emission originating

outside of star-forming regions. We also examine the effects of diffuse ionized gas, which is expected to account for a decreasing fraction of the nebular line emission toward higher redshifts, and argue that this is unlikely to be the dominant driver of the observed redshift evolution of $R_{\text{S II}}$ and of the derived n_e ([S II]) and $\log(P_{\text{th}}/k)$ ([S II]).

The galaxy spectra are stacked in bins of redshift and galaxy properties and the [S II] doublet ratio is used to measure the local n_e in the line-emitting gas. Based on these measurements, we find that:

1. The electron density of the line-emitting gas in SFGs has decreased by a factor of ~ 6 over the last ~ 10 Gyr. We measure n_e ([S II]) = 187_{-132}^{+140} cm⁻³ at $z \sim 2.2$, n_e ([S II]) = 79_{-40}^{+120} cm⁻³ at $z \sim 1.5$, n_e ([S II]) = 101_{-85}^{+59} cm⁻³ at $z \sim 0.9$, and n_e ([S II]) = 32_{-9}^{+4} cm⁻³ at $z \sim 0$, consistent with results from previous surveys of SFGs at similar redshifts.
2. Combining the SAMI and KMOS^{3D}+ data sets, we find that n_e ([S II]) shows roughly monotonic correlations with sSFR, SFR, and Σ_{SFR} across $0 \lesssim z \lesssim 2.6$. However, the KMOS^{3D}+ galaxies have systematically higher n_e than the SAMI galaxies at a fixed offset from the star-forming MS, suggesting that the n_e evolution is linked to the evolving main sequence normalization. There is also a roughly monotonic trend between n_e and Σ_{baryon} , but n_e is correlated with z at fixed Σ_* , suggesting that the gas reservoir plays an important role in regulating galaxy electron densities.

We investigate how the n_e ([S II]) measurements are impacted by contamination from nonstellar sources by comparing the [S II] ratios measured from the spectra of galaxies with outflows and/or AGN activity to the [S II] ratios measured for the primary sample. We measure higher n_e ([S II]) for inactive galaxies with outflows than for no-outflow inactive galaxies, but only $\sim 10\%$ – 30% of inactive SFGs at $0.6 < z < 2.6$ have outflows that are strong enough to be detectable in line emission, and this fraction is too low to have a significant impact on the measured average properties of the overall inactive SFG population. AGN host galaxies have lower [S II] ratios than inactive SFGs and should be excluded to avoid overestimating the average electron densities in star-forming regions.

We compare the local n_e ([S II]) measurements to estimates of the rms number of electrons per unit volume across star-forming disks at each redshift. The rms electron density n_e (rms) is calculated from the H α luminosity (which is proportional to the volume emission measure) and the line-emitting volume (which we define as $2\pi R_e^2 h$). The typical flattening ratios (R_e/h) of the high- z disks are estimated from the measured v_{rot}/σ_0 ratios. We find that n_e (rms) decreases by an order of magnitude from $z \sim 2.2$ to $z \sim 0$. The local and volume-averaged electron densities evolve at similar rates, suggesting that the volume filling factor of the line-emitting gas may be approximately constant across $0 \lesssim z \lesssim 2.6$.

Finally, we use our measurements of n_e ([S II]), $\log(P_{\text{th}}/k)$ ([S II]), and n_e (rms) to explore different potential drivers of the n_e evolution. We quantitatively test whether the electron density could plausibly be primarily governed by (a) the density of the parent molecular cloud, (b) the pressure injected by stellar feedback, (c) the pressure of the ambient medium, or (d) the dynamical evolution of the H II region. We find that n_e (rms) $\simeq n_{\text{H}_2}$, suggesting that the elevated electron

densities in H II regions at high- z could perhaps be the direct result of higher gas densities in the parent molecular clouds. There is also tentative evidence to suggest that n_e could be influenced by the balance between stellar feedback, which drives the expansion of H II regions, and the ambient pressure, which resists their expansion.

Further studies are required to confirm the feasibility of these scenarios. Our molecular gas mass estimates are based on scaling relations, and therefore, the relationships between n_e , n_{H_2} , and R_{stall} should be verified using samples of galaxies with both optical spectroscopy and molecular gas measurements. The H II region stall radii are estimated from analytic scalings that rely on many simplifying assumptions. Detailed comparisons between observed and predicted sizes for local H II regions would help to establish whether such scalings can be meaningfully applied to predict the typical sizes of ionized regions in more distant galaxies.

Our conclusions fit with the growing picture that the evolution of the properties of SFGs from the peak epoch of star formation to the present-day universe is primarily driven by a change in the rate of cold gas accretion onto galaxies. SFGs at $z \sim 2$ are thought to have elevated cold gas accretion rates, allowing them to maintain large molecular gas reservoirs that fuel rapid star formation, drive enhanced velocity dispersions, trigger the formation of massive clumps (see Tacconi et al. 2020 and Förster Schreiber & Wuyts 2020 for reviews), and based on our work, may also be responsible for the elevated electron densities in H II regions.

We thank the referee for their constructive report, which improved the clarity of this paper. R.L.D. would like to thank Barbara Catinella and Brent Groves for informative discussions. E.W. and J.T.M. acknowledge support by the Australian Research Council Centre of Excellence for All Sky Astrophysics in 3 Dimensions (ASTRO 3D), through project number CE170100013. M.F. acknowledges financial support from the European Research Council (ERC) under the European Union’s Horizon 2020 research and innovation program (grant agreement No. 757535). D.W. acknowledges the support of the Deutsche Forschungsgemeinschaft via Projects WI 3871/1-1 and WI 3871/1-2. Based on observations collected at the European Organisation for Astronomical Research in the Southern Hemisphere under ESO Programme IDs 073.B-9018, 074.A-9011, 075.A-0466, 076.A-0527, 077.A-0527, 078.A-0600, 079.A-0341, 080.A-0330, 080.A-0339, 080.A-0635, 081.A-0672, 081.B-0568, 082.A-0396, 183.A-0781, 087.A-0081, 088.A-0202, 088.A-0209, 090.A-0516, 091.A-0126, 092.A-0082, 092.A-0091, 093.A-0079, 093.A-0110, 093.A-0233, 094.A-0217, 094.A-0568, 095.A-0047, 096.A-0025, 097.A-0028, 098.A-0045, 099.A-0013, and 0100.A-0039. Also based on observations taken at the Large Binocular Telescope on Mt. Graham in Arizona. The LBT is an international collaboration among institutions in the United States, Italy, and Germany. LBT Corporation partners are The University of Arizona on behalf of the Arizona university system; Istituto Nazionale di Astrofisica, Italy; LBT Beteiligungsgesellschaft, Germany, representing the Max-Planck Society, the Astrophysical Institute Potsdam, and Heidelberg University; The Ohio State University, and The Research Corporation, on behalf of The University of Notre Dame, University of Minnesota and University of Virginia. This research made use of NASA’s Astrophysics Data System.

Software: ASTROPY (Astropy Collaboration et al. 2013, 2018), EMCEE (Foreman-Mackey et al. 2013), MATPLOTLIB (Hunter 2007), NUMPY (Oliphant 2006).

Appendix A

Impact of Sample Selection on the Measured Electron Densities

A.1. Star Formation Rate Bias

Our sample selection explicitly excludes AGN host galaxies and inactive galaxies with outflows because we are primarily interested in investigating what drives the evolution of the electron densities in H II regions over cosmic time. However, a significant fraction of the excluded galaxies are located at high stellar masses and/or above the star-forming MS, and as a result, the density sample has a slightly lower median SFR than the parent sample at fixed z (see Section 2.3). The most actively star-forming galaxies are expected to have the highest n_e (e.g., Shimakawa et al. 2015; Kaasinen et al. 2017; Jiang et al. 2019; Kashino & Inoue 2019), and therefore, the electron densities measured from the density sample could potentially underestimate the true average n_e in H II regions of $\log(M_*/M_\odot) \gtrsim 9-9.5$ galaxies at a given redshift.

We investigate the impact of the small SFR bias on the derived electron densities by estimating the average n_e of the narrow-line-emitting gas in different subsamples of galaxies with [S II]-clean spectra. We produce stacks including no-outflow inactive galaxies, AGN hosts, and/or inactive galaxies with outflows, and then fit the emission lines in the stacked spectra as superpositions of a narrow ISM component and a broader outflow component. The [S II] ratio of the narrow component can be used to calculate the average n_e in the disks of the stacked galaxies. However, a high-S/N detection of the outflow component is required to obtain a meaningful two-component decomposition of the emission-line profiles.

We perform the two-component emission-line fitting using EMCEE, a Markov Chain Monte Carlo (MCMC) Ensemble Sampler implemented in PYTHON (Foreman-Mackey et al. 2013). EMCEE returns the posterior probability distribution function (PDF) for each of the fit parameters and therefore allows us to evaluate whether or not the [S II] ratio of the narrow component is well constrained by the data. Within each kinematic component, all emission lines are tied to the same velocity offset and dispersion. We fit all five emission lines ([N II] λ 6548, H α , [N II] λ 6583, [S II] λ 6716, and [S II] λ 6731) simultaneously to obtain the best possible constraints on the kinematics of the two components. We adopt flat priors on all fit parameters and impose a top-hat prior on the [S II] ratio that has a value of 1 within the theoretically allowed range of $0.45 \leq R_{\text{S II}} \leq 1.45$ and 0 outside of this range. The MCMC is run with 300 walkers, 300 burn-in steps, and 1000 run steps.

We obtain meaningful two-component emission-line decompositions for stacks of galaxies at $z \sim 2.2$. At lower redshifts, the outflow emission is not strong enough to break degeneracies between the fit parameters. For the $z \sim 2.2$ stacks, we use the posterior PDFs of the emission-line narrow-component amplitudes to derive the posterior PDF of n_e following the method described in Section 2.6.2. From the stack of all inactive galaxies with [S II]-clean spectra at $z \sim 2.2$ (96 galaxies), we measure a disk n_e of $181_{-86}^{+123} \text{ cm}^{-3}$, and from the stack additionally including AGN host galaxies (110 galaxies in total), we measure a disk n_e of $207_{-100}^{+134} \text{ cm}^{-3}$. These

values are in very good agreement with the fiducial n_e measured from the density sample ($n_e = 187^{+140}_{-132} \text{ cm}^{-3}$). Förster Schreiber et al. (2019) performed similar two-component line fitting on the stack of the 33 inactive outflow host galaxies with the highest S/N spectra across $0.6 < z < 2.6$ (from the KMOS^{3D+} sample). They reported a narrow [S II] ratio of 1.33 ± 0.09 , almost identical to the ratio of 1.34 ± 0.03 obtained from the single-component fit to the stack of all no-outflow inactive galaxies in the same redshift range.²² Together, these results suggest that the electron densities measured from the stacks of no-outflow inactive galaxies are likely to reflect the average conditions in H II regions across the population of SFGs with $\log(M_*/M_\odot) \gtrsim 9-9.5$ at the probed redshifts.

A.2. Star-formation-driven Outflows

Recent observational results suggest that star-formation-driven ionized gas outflows at high redshift are approximately five times denser than the ionized ISM in the galaxies from which the outflows are launched (Förster Schreiber et al. 2019). The line emission from galaxies hosting outflows traces a combination of H II region gas and outflowing material, and therefore, the densities measured for these galaxies may be artificially enhanced and not representative of the conditions in H II regions. We compare the densities measured from single-component emission-line fits to stacked spectra of inactive galaxies with and without outflows (rather than the two-component fitting method described in Appendix A.1) and test how including galaxies hosting outflows in our stacks impacts the average density measured for each redshift slice.

The KMOS^{3D+} parent sample includes 87 inactive galaxies hosting outflows, of which 82 have spectra covering the [S II] doublet and 42 pass the quality control cut. Eight out of 42 fall in the $z \sim 0.9$ redshift slice, 3/42 fall in the $z \sim 1.5$ slice, and 31/42 fall in the $z \sim 2.2$ slice. Due to the relatively large sample variance (see, e.g., Table 1), at least ~ 10 galaxies are required to obtain a meaningful measurement of the average [S II] ratio, which in this case is only possible for the $z \sim 2.2$ subsample. Table 4 compares the pressures and densities measured for different subsamples of galaxies in each redshift slice. At $z \sim 2.2$, we measure somewhat higher densities and pressures in inactive galaxies with outflows compared to those with no outflows, although the two sets of measurements are consistent within the errors.²³

We also investigate how the inclusion of inactive galaxies hosting outflows in the primary sample would change the average measured pressure and density at each redshift. The fraction of inactive galaxies with outflows in our [S II]-clean sample is similar to the fraction in the KMOS^{3D+} parent sample. Galaxies hosting outflows account for 8/47 or 17% of

inactive galaxies in our $z \sim 0.9$ slice compared to 14% in the parent sample, 3/39 or 8% in our $z \sim 1.5$ slice compared to 13% in the parent sample, and 31/96 or 32% in our $z \sim 2.2$ slice compared to 29% in the parent sample. Therefore, the trends observed in our [S II]-clean sample should reflect the trends in the overall inactive galaxy population at $z \sim 0.9$ and $z \sim 2.2$, but may slightly underestimate the impact of outflows at $z \sim 1.5$. The measurements shown in Table 4 indicate that including inactive galaxies hosting outflows in the primary sample leads to modest enhancements in the inferred electron density (of up to $\sim 35 \text{ cm}^{-3}$) and ISM pressure (up to 0.2 dex), but the values derived from the full inactive sample and the no-outflow subsample are consistent within the errors. These results confirm that the increased incidence of star formation driven outflows at high z is unlikely to have a significant impact on the magnitude of the density evolution inferred from single-component Gaussian fits to the [S II] doublet lines.

The relatively small impact of outflows on the measured average densities can be explained by the modest fraction of inactive galaxies with detectable broad velocity components in their nebular emission-line profiles. The [S II] emission from the galaxies hosting outflows is a combination of an ISM component and an outflow component. For the $z \sim 2.2$ outflow galaxies, we measure a typical [S II] ratio of 1.16. Assuming that the outflow component has a typical [S II] ratio of 1.07 (as measured by Förster Schreiber et al. 2019) and that the ISM component has a typical [S II] ratio of 1.22 (as measured from our stack of no-outflow inactive galaxies), the measured [S II] ratio of 1.16 implies that $\sim 40\%$ of the [S II] flux originates from outflowing material. If we take this 40% outflow flux fraction and multiply it by the fraction of inactive galaxies with outflows (32% in our $z \sim 2.2$ slice), we would expect 13% of the [S II] emission from the full inactive galaxy population at $z \sim 2.2$ to be associated with outflowing material, corresponding to an expected [S II] ratio of ~ 1.20 —in very good agreement with the value measured from the “all inactive” stack. Performing a similar exercise for the $z \sim 1.5$ and $z \sim 0.9$ slices predicts that the average [S II] ratios in the overall inactive galaxy population should be 1.33 and 1.30, respectively, again in good agreement with the measured values.

Overall, we find that the presence of high-density outflowing material enhances the densities measured for galaxies hosting outflows over those measured for galaxies without outflows, but the incidence of outflows in the inactive galaxy population is not sufficient to have a significant impact on the measured average densities. The outflow fraction is highest at $z \sim 2.2$ ($\sim 30\%$), but at this redshift, the typical ISM density is only a factor of ~ 2 lower than the typical density of the outflowing material, with the consequence that including sources with outflows still has a limited impact on the measured average density.

A.3. AGN Contamination

There is growing observational evidence to suggest that AGN-driven outflows have [S II] densities of $\gtrsim 1000 \text{ cm}^{-3}$ (e.g., Perna et al. 2017; Kakkad et al. 2018; Förster Schreiber et al. 2019; Husemann et al. 2019; Shimizu et al. 2019); significantly denser than the ISM of typical inactive galaxies at high- z . Furthermore, outflows appear to be almost ubiquitous in AGN host galaxies at $z \sim 1-2$ (e.g., Förster Schreiber et al. 2014, 2019; Genzel et al. 2014; Harrison et al. 2016; Leung et al. 2019). We perform tests similar to those described in the

²² The narrow [S II] ratios reported by Förster Schreiber et al. (2019) are higher than those derived from our two-component fitting because they include galaxies across the full redshift range ($0.6 \lesssim z \lesssim 2.6$) whereas we focus only on galaxies at $1.9 \lesssim z \lesssim 2.6$.

²³ We note that the density measured from the outflow stack is $\sim 49 \text{ cm}^{-3}$ higher than the density measured from the no-outflow stack, but the ISM pressures derived from the two stacks differ by only 0.02 dex. This is because the outflow stack has a higher [N II]/H α ratio, which results in a higher inferred metallicity and a lower inferred electron temperature compared to the no-outflow stack. In reality, the enhanced [N II]/H α ratio in the outflow stack is likely due to a small contribution from shock excitation rather than a higher metallicity (e.g., Davies et al. 2019; Freeman et al. 2019), but this observation highlights the importance of accounting for metallicity differences between galaxy populations when studying ISM pressure.

Table 4Measured [S II] λ 6716/[S II] λ 6731, [S II]/H α and [N II]/H α Ratios and Calculated Metallicities, Electron Densities and Thermal Pressures for Different Subsamples of KMOS^{3D}+ Galaxies in Each Redshift Slice

Subsample	n_{gal}	$R_{\text{S II}}$	[N II]/H α	[S II]/H α	$12 + \log(\text{O}/\text{H})$	$\log(P/k)$	$n_e(\text{[S II]}) \text{ (cm}^{-3}\text{)}$
$z \sim 0.9$							
Inactive (no outflow)	39	$1.32^{+0.11}_{-0.08}$	0.19	0.23	8.50	$6.29^{+0.28}_{-0.73}$	101^{+59}_{-85}
Inactive (with outflow)	8			
All inactive	47	$1.27^{+0.10}_{-0.06}$	0.18	0.22	8.47	$6.48^{+0.14}_{-0.43}$	132^{+60}_{-83}
AGN hosts	3			
Inactive (no outflow) + AGN	42	$1.28^{+0.09}_{-0.09}$	0.20	0.24	8.51	$6.42^{+0.24}_{-0.39}$	123^{+87}_{-77}
$z \sim 1.5$							
Inactive (no outflow)	36	$1.34^{+0.05}_{-0.13}$	0.16	0.24	8.39	$6.23^{+0.43}_{-0.26}$	79^{+120}_{-40}
Inactive (with outflow)	3			
All inactive	39	$1.33^{+0.05}_{-0.13}$	0.16	0.24	8.39	$6.27^{+0.41}_{-0.22}$	89^{+120}_{-43}
AGN hosts	16	$1.18^{+0.11}_{-0.09}$			
Inactive (no outflow) + AGN	52	$1.25^{+0.07}_{-0.08}$	0.17	0.27	8.37	$6.58^{+0.16}_{-0.25}$	157^{+92}_{-53}
$z \sim 2.2$							
Inactive (no outflow)	65	$1.22^{+0.15}_{-0.10}$	0.15	0.19	8.47	$6.62^{+0.20}_{-0.53}$	187^{+140}_{-132}
Inactive (with outflow)	31	$1.16^{+0.17}_{-0.09}$	0.22	0.18	8.68	$6.64^{+0.16}_{-0.52}$	236^{+130}_{-160}
All inactive	96	$1.19^{+0.12}_{-0.07}$	0.18	0.19	8.56	$6.63^{+0.14}_{-0.37}$	207^{+104}_{-105}
AGN hosts	14	$1.11^{+0.26}_{-0.19}$			
Inactive (no outflow) + AGN	79	$1.22^{+0.13}_{-0.10}$	0.16	0.20	8.46	$6.61^{+0.17}_{-0.55}$	182^{+142}_{-122}

Note. In each section of the table, the top row gives the “fiducial” ISM pressure and electron density measured from the stack of inactive galaxies with no outflows. Subsequent rows list measurements for inactive galaxies with outflows and AGN host galaxies, and show how the density and pressure measurements change when these subpopulations are included in the primary sample. We did not make measurements for stacks with less than ten galaxies due to the relatively large sample variance. Densities and pressures are not calculated for AGN hosts because the H II region model grids that are used to convert from $R_{\text{S II}}$ to density and pressure cannot be meaningfully applied to spectra excited by nonstellar sources. Bold indicates the correct numbers to use in studies that might want to compare our results.

previous section to investigate the impact of AGN contamination on measurements of the ISM pressure and electron density at high z .

The KMOS^{3D}+ parent sample contains 136 AGN host galaxies, of which 112 have spectra covering the [S II] doublet. One of the galaxies is classified as a Type 1 AGN and excluded, and 33 of the remaining 111 galaxies pass the quality control cut. Three out of 33 fall in the $z \sim 0.9$ redshift slice, 16/33 fall in the $z \sim 1.5$ slice, and 14/33 fall in the $z \sim 2.2$ slice. We note that only 6/33 are classified as no-outflow systems (consistent with the high outflow fraction), so we analyze all of the AGN hosts together. AGN hosts account for 3/50 or 6% of galaxies in our $z \sim 0.9$ slice compared to 23% in the parent sample, 16/55 or 29% in our $z \sim 1.5$ slice compared to 29% in the parent sample, and 14/110 or 13% in our $z \sim 2.2$ slice compared to 20% in the parent sample. The AGN fraction in our [S II]-clean sample is very similar to the fraction in the parent sample for the $z \sim 1.5$ slice but is significantly lower than the fraction in the parent sample for the other two redshift slices, indicating that our tests may underestimate the true impact of AGN contamination in these redshift ranges.

The [S II] ratios measured for the AGN host galaxies in the $z \sim 1.5$ and $z \sim 2.2$ slices are listed in Table 4. We do not present density or pressure measurements for the AGN host galaxies because the grids that are used to convert the [S II] ratios to densities and pressures are outputs of H II region photoionization models. The hard ionizing radiation field of the AGN will change the ionization and temperature structure of the nebula, resulting in

a different relationship between $R_{\text{S II}}$ and density/pressure. AGN host galaxies appear to have lower [S II] ratios than inactive galaxies with and without outflows at the same redshift, although the differences between the line ratios measured for the different $z \sim 2.2$ stacks are not statistically significant. There is some evidence to suggest that AGN contamination may impact the measured ISM densities and pressures, particularly in the $z \sim 1.5$ slice where both quantities increase by a factor of ~ 2 when AGNs are included. The inclusion of AGN host galaxies has only a minor impact on measured average density in the $z \sim 0.9$ redshift slice and does not have any significant impact on the measurements in the $z \sim 2.2$ slice, but we emphasize that for these redshift slices, the AGN fractions in our [S II]-clean sample are a factor of ~ 2 –4 lower than in the parent sample, and therefore our test likely only provides a lower limit on the impact of AGN contamination.

In studies of high-redshift star-forming galaxies, AGN are commonly identified using X-ray, radio, and/or mid-IR data. However, Förster Schreiber et al. (2019) showed that these classical selection techniques may miss up to $\sim 50\%$ of AGNs at $z \sim 1$ –2, likely due to both the varying availability and depth of ancillary data between different extragalactic fields, and the impact of AGN variability and small-scale nuclear obscuration on the different diagnostic tracers (e.g., Padovani et al. 2017). Our results indicate that it is important to use conservative AGN selection criteria (e.g., including optical line ratios) to minimize the probability of contamination from nonstellar excitation sources when measuring electron densities and ISM pressures.

Table 5
Literature Samples

Sample/Reference	Median z	Median $\log(M_*/M_\odot)$	Median SFR ($M_\odot \text{ yr}^{-1}$)	Density Diagnostic	Line Ratio	n_e (cm^{-3})
KROSS (Swinbank et al. 2019)	0.85	10.0	6.7	[S II]	1.4 ± 0.1	33^{+78}_{-32}
COSMOS-[O II] (Kaasinen et al. 2017)	1.5	10.6	26.4	[O II]	1.29 ± 0.03	119^{+24}_{-21}
FMOS-COSMOS (Kashino et al. 2017)	1.55	10.2	$\sim 59^a$	[S II]	1.21 ± 0.1	193^{+150}_{-88}
MOSDEF (Sanders et al. 2016)	2.24	10.1	29.7	[S II]	$1.13^{+0.16}_{-0.06}$	316^{+92}_{-197}
KBSS-MOSFIRE (Steidel et al. 2014)	2.3	10.0	23.3	[O II]	1.16 ± 0.04	258^{+67}_{-56}

Notes. Line-ratio measurements were taken directly from the listed references and electron densities were recalculated adopting the metallicity of the KMOS^{3D} stack lying closest in redshift. In cases where both the [S II] and the [O II] ratio were quoted, we calculate the density from the [S II] ratio for consistency with our analysis. ^a From Figure 1 of Kashino et al. (2017), we estimated that their H α -detected sample has a median SFR of $\sim 100 M_\odot \text{ yr}^{-1}$. Their SFRs were calculated assuming a Salpeter IMF, so we divided by 1.7 to convert to a Chabrier IMF, yielding the $\sim 59 M_\odot \text{ yr}^{-1}$ quoted here.

Appendix B High- z Literature Samples

We supplement our KMOS^{3D}+ results with measurements from other surveys of high- z galaxies in the literature. Specifically, we select samples of galaxies at $z \gtrsim 0.6$ that lie within ~ 0.5 dex of the Speagle et al. (2014) star-forming MS and have published [S II] $\lambda 6716$ /[S II] $\lambda 6731$ or [O II] $\lambda 3726$ /[O II] $\lambda 3729$ measurements. All stellar masses and SFRs are scaled to the Chabrier (2003) initial mass function for consistency with our measurements. We require published line ratios to avoid systematic biases in the conversion between line ratios and densities arising from differences in the atomic data or assumed electron temperature (see, e.g., discussions in Sanders et al. 2016; Kewley et al. 2019). We only include data sets with at least 20 galaxies to minimize the impact of variance within the galaxy population. Our final high- z comparison sample contains measurements from KROSS (Swinbank et al. 2019), COSMOS-[O II] (Kaasinen et al. 2017), FMOS-COSMOS (Kashino et al. 2017), MOSDEF (Sanders et al. 2016), and KBSS-MOSFIRE (Steidel et al. 2014). Table 5 summarizes the properties of the high- z literature samples as well as the line-ratio measurements and the derived electron densities. We do not have size measurements for the galaxies in these samples, so the average surface density quantities used in Figures 6 and 7 are estimated assuming that the galaxies lie on the redshift-dependent mass–size relation from van der Wel et al. (2014).

Appendix C

Constraints on Atomic Gas Reservoirs at $z \sim 1-3$

The redshift evolution of galaxy atomic gas reservoirs is poorly constrained because current radio telescopes can only detect HI emission from galaxies at $z \lesssim 0.4$. At higher redshifts, the atomic gas mass volume density can be estimated from Ly α absorption in quasar spectra, but this probes gas both in galaxies and in the circumgalactic medium around galaxies. Current observational compilations suggest that the neutral hydrogen volume density of the universe has decreased by a factor of ~ 1.5 since $z \sim 2$ (see Péroux & Howk 2020 and references therein), whereas the molecular hydrogen volume density has decreased by a factor of ~ 4 (e.g., Decarli et al. 2016; Scoville et al. 2017; Riechers et al. 2019; Lenkić et al. 2020; Tacconi et al. 2020). Therefore, the fraction of the ISM in the molecular phase is expected to increase toward higher redshifts.

HI mapping surveys of local spiral galaxies have found that Σ_{HI} has a relatively constant value of $\sim 6 M_\odot \text{ pc}^{-2}$ at all galactocentric radii (e.g., Leroy et al. 2008) and rarely exceeds $\sim 10 M_\odot \text{ pc}^{-2}$ (e.g., Bigiel et al. 2008; Leroy et al. 2008; Schruba et al. 2018), most likely because HI is converted to H₂ at higher gas mass surface densities (see, e.g., discussion in Tacconi et al. 2020). The maximal Σ_{HI} is inversely correlated with the gas-phase metallicity (e.g., Schruba et al. 2018). The metallicities measured from our four stacked spectra (see Section 2.6.2) are consistent with each other within 0.1 dex, because the average stellar mass of the probed galaxies increases toward higher redshifts. Therefore, the maximal Σ_{HI} is not expected to vary significantly between our samples. On the other hand, Σ_{H_2} increases from the outskirts to the centers of local spiral galaxies and no saturation is observed (e.g., Schruba et al. 2011).

There is a tight relationship between the masses and diameters of local HI disks which implies a uniform characteristic Σ_{HI} of $6.9 M_\odot \text{ pc}^{-2}$ (Broeils & Rhee 1997; Wang et al. 2016; assuming a standard helium mass fraction of 36%). In comparison, the Tacconi et al. (2020) molecular gas depletion time scaling relation suggests that the SAMI and KMOS^{3D}+ galaxies have median molecular gas mass surface densities of $\sim 8 M_\odot \text{ pc}^{-2}$ and $\sim 200 M_\odot \text{ pc}^{-2}$, respectively (see Figure 7). The typical Σ_{H_2} for the KMOS^{3D}+ galaxies is more than an order of magnitude above the surface density at which Σ_{HI} is observed to saturate in local galaxies, suggesting that the ISM in the central regions of high- z SFGs is likely to be strongly dominated by molecular gas. On the other hand, the gas reservoirs within R_e for the SAMI galaxies are likely to be approximately equal parts HI and H₂. We adopt $\Sigma_{\text{HI}} = 6.9 M_\odot \text{ pc}^{-2}$ at all redshifts but note that the average total gas mass surface densities of the KMOS^{3D}+ galaxies are insensitive to the adopted Σ_{HI} within any reasonable range of values. Varying Σ_{HI} by a factor of 2 would change the median midplane pressure at $z \sim 0$ (Section 5.3) by $\lesssim 0.2$ dex and the inverse of the HII region stall radius (Section 5.4) by $\lesssim 0.15$ dex.

Appendix D

Stellar Velocity Dispersion Estimates

For a disk in hydrostatic equilibrium, the vertical stellar velocity dispersion is given by

$$\sigma_{*,z} = h_* \sqrt{2\pi G \rho}, \quad (\text{D1})$$

where h_* is the scale height of the stellar disk and ρ is the midplane mass volume density (van der Kruit 1988; Leroy et al. 2008). We assume that, for the relatively high-mass galaxies considered in this analysis, ρ is dominated by the stellar and gas components.

In the local universe, the average “flattening” (ratio of scale length to scale height, $R_{d,*}/h_*$) of the stellar disk is 7.3 (Kregel et al. 2002; Sun et al. 2020). For the SAMI galaxies at $z \sim 0$, we adopt $h_* = R_{d,*}/7.3$ and approximate $R_{d,*}$ from R_e using the relationship for an exponential disk ($R_{d,*} \simeq R_e/1.67$).

High- z disks are significantly thicker than $z \sim 0$ disks, both photometrically (e.g., Elmegreen et al. 2017) and kinematically (e.g., Förster Schreiber et al. 2009; Wisnioski et al. 2015; Johnson et al. 2018), and therefore, we cannot use the $z \sim 0$ flattening to derive h_* from R_e . Instead, we assume that the stellar scale heights of the KMOS^{3D+} galaxies are approximately equivalent to their ionized gas scale heights. This is plausibly a reasonable assumption (to first order) given that the majority of the ionized gas is likely to be associated with H II regions (see discussion in Section 3.4.2) and that the stellar populations of galaxies at $z \sim 1-2$ must be relatively young. The scale heights of stellar disks increase over time as a result of mergers and gravitational interactions with massive objects in the disk (such as giant molecular clouds, globular clusters, and black holes). These encounters randomly perturb the momentum of individual stars, leading to the diffusion of stellar orbits and an increase in the vertical velocity dispersion and scale height of the stellar disk (e.g., Wielen 1977). The scale height of the star-forming disk also changes over time (see discussion in Section 3.4.3). Therefore, the stellar and ionized gas scale heights will be most similar in galaxies with young stellar populations. We note that varying h_* by a factor of 2 changes the midplane pressures derived in Section 5.3 by <0.15 dex, and therefore, the uncertainties on h_* have a relatively limited impact on our results.

We have a single value of ρ per galaxy, which can be used to estimate the average stellar velocity dispersion within R_e . We assume that the scale height is constant as a function of radius (for consistency with the $n_e(\text{rms})$ calculations in Section 3.4), but note that the average scale height within R_e for a flared disk (i.e., with constant disk velocity dispersion; e.g., Burkert et al. 2010) is almost identical to the scale height at R_d , and therefore, the choice of geometry has a negligible impact on the derived midplane pressure.

Appendix E

Derivation of H II Region Stall Radius

The time evolution of the internal pressure of an adiabatically expanding bubble driven by stellar winds and supernovae is given in Equation (25) of Oey & Clarke (1997):

$$P_{\text{int}}(t) = \frac{7}{(3850\pi)^{2/5}} L_{\text{mech}}^{2/5} \rho_0^{3/5} t^{-4/5}, \quad (\text{E1})$$

where L_{mech} is the mechanical luminosity of the central star cluster and ρ_0 is the mass volume density of the material surrounding the H II region. Assuming that the expansion of the bubble stalls when P_{int} reaches the ambient pressure P_0 , the stall time t_{stall} is related to L_{mech} , ρ_0 , and P_0 as follows:

$$t_{\text{stall}} \propto L_{\text{mech}}^{1/2} \rho_0^{3/4} P_0^{-5/4}. \quad (\text{E2})$$

The time evolution of the radius of the expanding bubble is given in Equation (24) of Oey & Clarke (1997):

$$R(t) = \left(\frac{250}{308\pi} \right)^{1/5} L_{\text{mech}}^{1/5} \rho_0^{-1/5} t^{3/5}. \quad (\text{E3})$$





















The expression for the stall time (Equation (E2)) can be substituted into Equation (E3) to derive the stall radius R_{stall} as a function of L_{mech} , ρ_0 , and P_0 :

$$\begin{aligned} R_{\text{stall}} &\propto L_{\text{mech}}^{1/5} \rho_0^{-1/5} (L_{\text{mech}}^{1/2} \rho_0^{3/4} P_0^{-5/4})^{3/5} \\ &\propto L_{\text{mech}}^{1/2} \rho_0^{1/4} P_0^{-3/4}. \end{aligned} \quad (\text{E4})$$

We assume that the ambient pressure is equivalent to the hydrostatic equilibrium midplane pressure P_{mid} (discussed in Section 5.3), that the mechanical luminosity of the central star cluster is proportional to Σ_{SFR} (discussed in Section 5.2), and that the mass volume density of the material surrounding the H II region is proportional to ρ_{H_2} (discussed in Section 5.1). Under these conditions, the stall radius can be expressed as

$$R_{\text{stall}} \propto \Sigma_{\text{SFR}}^{1/2} \rho_{\text{H}_2}^{1/4} P_{\text{mid}}^{-3/4}. \quad (\text{E5})$$

ORCID iDs

Rebecca L. Davies  <https://orcid.org/0000-0002-3324-4824>
 R. Genzel  <https://orcid.org/0000-0002-2767-9653>
 T. T. Shimizu  <https://orcid.org/0000-0002-2125-4670>
 R. I. Davies  <https://orcid.org/0000-0003-4949-7217>
 L. J. Tacconi  <https://orcid.org/0000-0002-1485-9401>
 H. Übler  <https://orcid.org/0000-0003-4891-0794>
 E. Wisnioski  <https://orcid.org/0000-0003-1657-7878>
 S. Wuyts  <https://orcid.org/0000-0003-3735-1931>
 M. Fossati  <https://orcid.org/0000-0002-9043-8764>
 D. Lutz  <https://orcid.org/0000-0003-0291-9582>
 J. T. Mendel  <https://orcid.org/0000-0002-6327-9147>
 T. Naab  <https://orcid.org/0000-0002-7314-2558>
 S. H. Price  <https://orcid.org/0000-0002-0108-4176>
 A. Renzini  <https://orcid.org/0000-0002-7093-7355>
 D. Wilman  <https://orcid.org/0000-0002-1822-4462>
 A. Beifiori  <https://orcid.org/0000-0001-8017-6097>
 S. Belli  <https://orcid.org/0000-0002-5615-6018>
 A. Burkert  <https://orcid.org/0000-0001-6879-9822>
 J. Chan  <https://orcid.org/0000-0001-6251-3125>
 M. M. Lee  <https://orcid.org/0000-0002-2419-3068>
 R. P. Saglia  <https://orcid.org/0000-0003-0378-7032>

References

- Acharyya, A., Kewley, L. J., Rigby, J. R., et al. 2019, *MNRAS*, **488**, 5862
 Arribas, S., Colina, L., Bellocchi, E., Maiolino, R., & Villar-Martín, M. 2014, *A&A*, **568**, A14
 Astropy Collaboration, Price-Whelan, A. M., Sipőcz, B. M., et al. 2018, *AJ*, **156**, 18
 Astropy Collaboration, Robitaille, T. P., Tollerud, E. J., et al. 2013, *A&A*, **558**, A33
 Bagetakos, I., Brinks, E., Walter, F., et al. 2011, *AJ*, **141**, 23
 Bayliss, M. B., Rigby, J. R., Sharon, K., et al. 2014, *ApJ*, **790**, 144
 Begelman, M. C. 1990, in *Thermal Phases of the Interstellar Medium in Galaxies*, ed. J. Thronson, A. Harley, & J. M. Shull (Dordrecht: Kluwer), 287
 Berg, D. A., Skillman, E. D., Croxall, K. V., et al. 2015, *ApJ*, **806**, 16
 Bian, F., Fan, X., Bechtold, J., et al. 2010, *ApJ*, **725**, 1877
 Bian, F., Kewley, L. J., Dopita, M. A., & Juneau, S. 2016, *ApJ*, **822**, 62
 Bian, F., Kewley, L. J., Groves, B., & Dopita, M. A. 2020, *MNRAS*, **493**, 580

- Bigiel, F., Leroy, A., Walter, F., et al. 2008, *AJ*, **136**, 2846
- Binette, L., González-Gómez, D. I., & Mayya, Y. D. 2002, *RMxAA*, **38**, 279
- Bizyaev, D., Walterbos, R. A. M., Yoachim, P., et al. 2017, *ApJ*, **839**, 87
- Bournaud, F., Elmegreen, B. G., & Elmegreen, D. M. 2007, *ApJ*, **670**, 237
- Broeils, A. H., & Rhee, M. H. 1997, *A&A*, **324**, 877
- Bryant, J. J., Owers, M. S., Robotham, A. S. G., et al. 2015, *MNRAS*, **447**, 2857
- Bundy, K., Bershady, M. A., Law, D. R., et al. 2015, *ApJ*, **798**, 7
- Burkert, A., Genzel, R., Bouché, N., et al. 2010, *ApJ*, **725**, 2324
- Caldú-Primo, A., Schruha, A., Walter, F., et al. 2013, *AJ*, **146**, 150
- Cappellari, M. 2017, *MNRAS*, **466**, 798
- Cappellari, M., & Emsellem, E. 2004, *PASP*, **116**, 138
- Castor, J., McCray, R., & Weaver, R. 1975, *ApJL*, **200**, L107
- Cedrés, B., Beckman, J. E., Bongiovanni, Á., et al. 2013, *ApJL*, **765**, L24
- Chabrier, G. 2003, *PASP*, **115**, 763
- Chevance, M., Kruijssen, J. M. D., Hygate, A. P. S., et al. 2020, *MNRAS*, **493**, 2872
- Christensen, L., Laursen, P., Richard, J., et al. 2012, *MNRAS*, **427**, 1973
- Cresci, G., Hicks, E. K. S., Genzel, R., et al. 2009, *ApJ*, **697**, 115
- Daddi, E., Dickinson, M., Morrison, G., et al. 2007, *ApJ*, **670**, 156
- D'Agostino, J. J., Kewley, L. J., Groves, B., et al. 2019, *ApJ*, **878**, 2
- Davies, R., Baron, D., Shimizu, T., et al. 2020, *MNRAS*, **498**, 4150
- Davies, R. L., Förster Schreiber, N. M., Übler, H., et al. 2019, *ApJ*, **873**, 122
- Decarli, R., Walter, F., Aravena, M., et al. 2016, *ApJ*, **833**, 69
- Dekel, A., Sari, R., & Ceverino, D. 2009, *ApJ*, **703**, 785
- Della Bruna, L., Adamo, A., Bik, A., et al. 2020, *A&A*, **635**, A134
- Dopita, M. A., Fischera, J., Sutherland, R. S., et al. 2006, *ApJS*, **167**, 177
- Dopita, M. A., Kewley, L. J., Sutherland, R. S., & Nicholls, D. C. 2016, *Ap&SS*, **361**, 61
- Dopita, M. A., & Sutherland, R. S. 2003, *Astrophysics of the Diffuse Universe* (New York: Springer)
- Dorland, H., & Montmerle, T. 1987, *A&A*, **177**, 243
- Dyson, J. E., & Williams, D. A. 1980, *Physics of the Interstellar Medium* (Manchester: Univ. Press)
- Elbaz, D., Daddi, E., Le Borgne, D., et al. 2007, *A&A*, **468**, 33
- Elmegreen, B. G. 1989, *ApJ*, **338**, 178
- Elmegreen, B. G., & Elmegreen, D. M. 2005, *ApJ*, **627**, 632
- Elmegreen, B. G., Elmegreen, D. M., Tompkins, B., & Jenks, L. G. 2017, *ApJ*, **847**, 14
- Elmegreen, B. G., & Hunter, D. A. 2000, *ApJ*, **540**, 814
- Erb, D. K., Shapley, A. E., Pettini, M., et al. 2006, *ApJ*, **644**, 813
- Field, G. B. 1965, *ApJ*, **142**, 531
- Fluetsch, A., Maiolino, R., Carniani, S., et al. 2020, arXiv:2006.13232
- Foreman-Mackey, D., Hogg, D. W., Lang, D., & Goodman, J. 2013, *PASP*, **125**, 306
- Förster Schreiber, N. M., Genzel, R., Bouché, N., et al. 2009, *ApJ*, **706**, 1364
- Förster Schreiber, N. M., Genzel, R., Lutz, D., Kunze, D., & Sternberg, A. 2001, *ApJ*, **552**, 544
- Förster Schreiber, N. M., Genzel, R., Newman, S. F., et al. 2014, *ApJ*, **787**, 38
- Förster Schreiber, N. M., Renzini, A., Mancini, C., et al. 2018, *ApJS*, **238**, 21
- Förster Schreiber, N. M., Übler, H., Davies, R. L., et al. 2019, *ApJ*, **875**, 21
- Förster Schreiber, N. M., & Wuyts, Stijn 2020, *ARA&A*, **58**, 661
- Freeman, W. R., Siana, B., Kriek, M., et al. 2019, *ApJ*, **873**, 102
- Genel, S., Naab, T., Genzel, R., et al. 2012, *ApJ*, **745**, 11
- Gentry, E. S., Krumholz, M. R., Madau, P., & Lupi, A. 2019, *MNRAS*, **483**, 3647
- Genzel, R., Burkert, A., Bouché, N., et al. 2008, *ApJ*, **687**, 59
- Genzel, R., Förster Schreiber, N. M., Rosario, D., et al. 2014, *ApJ*, **796**, 7
- Genzel, R., Newman, S., Jones, T., et al. 2011, *ApJ*, **733**, 101
- Genzel, R., Schreiber, N. M. F., Übler, H., et al. 2017, *Natur*, **543**, 397
- Genzel, R., Tacconi, L. J., Eisenhauer, F., et al. 2006, *Natur*, **442**, 786
- Genzel, R., Tacconi, L. J., Kurk, J., et al. 2013, *ApJ*, **773**, 68
- Genzel, R., Tacconi, L. J., Lutz, D., et al. 2015, *ApJ*, **800**, 20
- Groves, B., Dopita, M. A., Sutherland, R. S., et al. 2008, *ApJS*, **176**, 438
- Gutiérrez, L., & Beckman, J. E. 2010, *ApJL*, **710**, L44
- Haffner, L. M., Reynolds, R. J., & Tufte, S. L. 1999, *ApJ*, **523**, 223
- Hainline, K. N., Shapley, A. E., Kornei, K. A., et al. 2009, *ApJ*, **701**, 52
- Harper-Clark, E., & Murray, N. 2009, *ApJ*, **693**, 1696
- Harrison, C. M., Alexander, D. M., Mullaney, J. R., et al. 2016, *MNRAS*, **456**, 1195
- Herrera-Camus, R., Bolatto, A., Smith, J. D., et al. 2016, *ApJ*, **826**, 175
- Ho, I.-T., Kewley, L. J., Dopita, M. A., et al. 2014, *MNRAS*, **444**, 3894
- Ho, I.-T., Kudritzki, R.-P., Kewley, L. J., et al. 2015, *MNRAS*, **448**, 2030
- Hunt, L. K., & Hirashita, H. 2009, *A&A*, **507**, 1327
- Hunter, J. D. 2007, *CSE*, **9**, 90
- Husemann, B., Scharwächter, J., Davis, T. A., et al. 2019, *A&A*, **627**, A53
- Jiang, T., Malhotra, S., Yang, H., & Rhoads, J. E. 2019, *ApJ*, **872**, 146
- Johnson, H. L., Harrison, C. M., Swinbank, A. M., et al. 2018, *MNRAS*, **474**, 5076
- Jones, T., Martin, C., & Cooper, M. C. 2015, *ApJ*, **813**, 126
- Kaasinen, M., Bian, F., Groves, B., Kewley, L. J., & Gupta, A. 2017, *MNRAS*, **465**, 3220
- Kaasinen, M., Kewley, L., Bian, F., et al. 2018, *MNRAS*, **477**, 5568
- Kakkad, D., Groves, B., Dopita, M., et al. 2018, *A&A*, **618**, A6
- Kashino, D., & Inoue, A. K. 2019, *MNRAS*, **486**, 1053
- Kashino, D., Silverman, J. D., Sanders, D., et al. 2017, *ApJ*, **835**, 88
- Kauffmann, G., Heckman, T. M., Tremonti, C., et al. 2003, *MNRAS*, **346**, 1055
- Kelvin, L. S., Driver, S. P., Robotham, A. S. G., et al. 2012, *MNRAS*, **421**, 1007
- Kennicutt, R. C., Jr. 1984, *ApJ*, **287**, 116
- Kewley, L. J., Dopita, M. A., Leitherer, C., et al. 2013, *ApJ*, **774**, 100
- Kewley, L. J., Groves, B., Kauffmann, G., & Heckman, T. 2006, *MNRAS*, **372**, 961
- Kewley, L. J., Nicholls, D. C., Sutherland, R., et al. 2019, *ApJ*, **880**, 16
- Kim, C.-G., & Ostriker, E. C. 2015, *ApJ*, **802**, 99
- Kim, D.-C., Evans, A. S., Vavilkin, T., et al. 2013, *ApJ*, **768**, 102
- Kim, K.-T., & Koo, B.-C. 2001, *ApJ*, **549**, 979
- Kreckel, K., Ho, I. T., Blanc, G. A., et al. 2019, *ApJ*, **887**, 80
- Kregel, M., van der Kruit, P. C., & de Grijs, R. 2002, *MNRAS*, **334**, 646
- Kriek, M., van Dokkum, P. G., Franx, M., et al. 2007, *ApJ*, **669**, 776
- Kriek, M., van Dokkum, P. G., Franx, M., et al. 2008, *ApJ*, **677**, 219
- Kruijssen, J. M. D., Schruha, A., Chevance, M., et al. 2019, *Natur*, **569**, 519
- Krumholz, M. R., & Burkhardt, B. 2016, *MNRAS*, **458**, 1671
- Krumholz, M. R., Burkhardt, B., Forbes, J. C., & Crocker, R. M. 2018, *MNRAS*, **477**, 2716
- Krumholz, M. R., & Matzner, C. D. 2009, *ApJ*, **703**, 1352
- Lang, P., Wuyts, S., Somerville, R. S., et al. 2014, *ApJ*, **788**, 11
- Law, D. R., Steidel, C. C., Erb, D. K., et al. 2009, *ApJ*, **697**, 2057
- Lenkić, L., Bolatto, A. D., Förster Schreiber, N. M., et al. 2020, *AJ*, **159**, 190
- Leroy, A. K., Walter, F., Brinks, E., et al. 2008, *AJ*, **136**, 2782
- Leung, G. C. K., Coil, A. L., Aird, J., et al. 2019, *ApJ*, **886**, 11
- Levy, R. C., Bolatto, A. D., Sánchez, S. F., et al. 2019, *ApJ*, **882**, 84
- Levy, R. C., Bolatto, A. D., Teuben, P., et al. 2018, *ApJ*, **860**, 92
- Liu, D., Schinnerer, E., Groves, B., et al. 2019, *ApJ*, **887**, 235
- Liu, X., Shapley, A. E., Coil, A. L., Brinchmann, J., & Ma, C.-P. 2008, *ApJ*, **678**, 758
- Lopez, L. A., Krumholz, M. R., Bolatto, A. D., et al. 2014, *ApJ*, **795**, 121
- Madau, P., & Dickinson, M. 2014, *ARA&A*, **52**, 415
- Madsen, G. J., Reynolds, R. J., & Haffner, L. M. 2006, *ApJ*, **652**, 401
- Mancini, C., Förster Schreiber, N. M., Renzini, A., et al. 2011, *ApJ*, **743**, 86
- Martin, C. L. 1997, *ApJ*, **491**, 561
- Masters, D., Faisst, A., & Capak, P. 2016, *ApJ*, **828**, 18
- Masters, D., McCarthy, P., Siana, B., et al. 2014, *ApJ*, **785**, 153
- McKee, C. F., van Buren, D., & Lazareff, B. 1984, *ApJL*, **278**, L115
- McLeod, A. F., Dale, J. E., Evans, C. J., et al. 2019, *MNRAS*, **486**, 5263
- McLeod, A. F., Dale, J. E., Ginsburg, A., et al. 2015, *MNRAS*, **450**, 1057
- McLeod, A. F., Kruijssen, J. M. D., Weisz, D. R., et al. 2020, *ApJ*, **891**, 25
- Medling, A. M., Cortese, L., Croom, S. M., et al. 2018, *MNRAS*, **475**, 5194
- Millard, J. S., Eales, S. A., Smith, M. W. L., et al. 2020, *MNRAS*, **494**, 293
- Miller, S. T., & Veilleux, S. 2003, *ApJS*, **148**, 383
- Moustakas, J., Kennicutt, R. C., Jr., Tremonti, C. A., et al. 2010, *ApJS*, **190**, 233
- Murray, N., Quataert, E., & Thompson, T. A. 2010, *ApJ*, **709**, 191
- Nakajima, K., & Ouchi, M. 2014, *MNRAS*, **442**, 900
- Nath, B. B., Das, P., & Oey, M. S. 2020, *MNRAS*, **493**, 1034
- Nelson, E. J., van Dokkum, P. G., Förster Schreiber, N. M., et al. 2016a, *ApJ*, **828**, 27
- Nelson, E. J., van Dokkum, P. G., Momcheva, I., et al. 2013, *ApJL*, **763**, L16
- Nelson, E. J., van Dokkum, P. G., Momcheva, I. G., et al. 2016b, *ApJL*, **817**, L9
- Newman, S. F., Buschkamp, P., Genzel, R., et al. 2014, *ApJ*, **781**, 21
- Newman, S. F., Genzel, R., Förster Schreiber, N. M., et al. 2013, *ApJ*, **767**, 104
- Newman, S. F., Genzel, R., Förster-Schreiber, N. M., et al. 2012, *ApJ*, **761**, 43
- Oey, M. S., & Clarke, C. J. 1997, *MNRAS*, **289**, 570
- Oey, M. S., & Clarke, C. J. 1998, *Magellanic Clouds and Other Dwarf Galaxies*, **185**
- Oey, M. S., Meurer, G. R., Yelda, S., et al. 2007, *ApJ*, **661**, 801
- Oliphant, T. E. 2006, *A Guide to NumPy*, Vol. 1 (USA: Trelgol Publishing)
- Osterbrock, D., & Flather, E. 1959, *ApJ*, **129**, 26
- Osterbrock, D. E., & Ferland, G. J. 2006, *Astrophysics of Gaseous Nebulae and Active Galactic Nuclei* (Sausalito, CA: Univ. Science Books)

- Ostriker, E. C., & Shetty, R. 2011, *ApJ*, 731, 41
- Padovani, P., Alexander, D. M., Assef, R. J., et al. 2017, *A&ARv*, 25, 2
- Pellegrini, E. W., Oey, M. S., Winkler, P. F., et al. 2012, *ApJ*, 755, 40
- Perna, M., Lanzuisi, G., Brusa, M., Cresci, G., & Mignoli, M. 2017, *A&A*, 606, A96
- Péroux, C., & Howk, J. C. 2020, *ARA&A*, 58, 363
- Pety, J., Schinnerer, E., Leroy, A. K., et al. 2013, *ApJ*, 779, 43
- Phillips, J. P. 2007, *MNRAS*, 380, 369
- Poetrodjojo, H., D'Agostino, J. J., Groves, B., et al. 2019, *MNRAS*, 487, 79
- Poetrodjojo, H., Groves, B., Kewley, L. J., et al. 2018, *MNRAS*, 479, 5235
- Proxauf, B., Öttl, S., & Kimeswenger, S. 2014, *A&A*, 561, A10
- Puglisi, A., Daddi, E., Renzini, A., et al. 2017, *ApJL*, 838, L18
- Rahner, D., Pellegrini, E. W., Glover, S. C. O., & Klessen, R. S. 2017, *MNRAS*, 470, 4453
- Rahner, D., Pellegrini, E. W., Glover, S. C. O., & Klessen, R. S. 2019, *MNRAS*, 483, 2547
- Ramirez-Ballinas, I., & Hidalgo-Gómez, A. M. 2014, *MNRAS*, 442, 2282
- Rand, R. J. 1998, *ApJ*, 501, 137
- Reynolds, R. J. 1991, *ApJL*, 372, L17
- Riechers, D. A., Pavesi, R., Sharon, C. E., et al. 2019, *ApJ*, 872, 7
- Rigby, J. R., Wuyts, E., Gladders, M. D., Sharon, K., & Becker, G. D. 2011, *ApJ*, 732, 59
- Rossa, J., & Dettmar, R. J. 2003, *A&A*, 406, 493
- Sanders, R. L., Jones, T., Shapley, A. E., et al. 2020, *ApJL*, 888, L11
- Sanders, R. L., Shapley, A. E., Kriek, M., et al. 2016, *ApJ*, 816, 23
- Sanders, R. L., Shapley, A. E., Zhang, K., & Yan, R. 2017, *ApJ*, 850, 136
- Schaefer, A. L., Croom, S. M., Allen, J. T., et al. 2017, *MNRAS*, 464, 121
- Schruba, A., Bialy, S., & Sternberg, A. 2018, *ApJ*, 862, 110
- Schruba, A., Leroy, A. K., Walter, F., et al. 2011, *AJ*, 142, 37
- Scott, N., van de Sande, J., Croom, S. M., et al. 2018, *MNRAS*, 481, 2299
- Scoville, N., Lee, N., Vanden Bout, P., et al. 2017, *ApJ*, 837, 150
- Scoville, N. Z., Thakkar, D., Carlstrom, J. E., & Sargent, A. I. 1993, *ApJL*, 404, L59
- Shapley, A. E., CoiSoto17l, A. L., Ma, C.-P., & Bundy, K. 2005, *ApJ*, 635, 1006
- Shapley, A. E., Reddy, N. A., Kriek, M., et al. 2015, *ApJ*, 801, 88
- Shapley, A. E., Sanders, R. L., Shao, P., et al. 2019, *ApJL*, 881, L35
- Shimakawa, R., Kodama, T., Steidel, C. C., et al. 2015, *MNRAS*, 451, 1284
- Shimizu, T. T., Davies, R. I., Lutz, D., et al. 2019, *MNRAS*, 490, 5860
- Shirazi, M., Vegetti, S., Nesvadba, N., et al. 2014, *MNRAS*, 440, 2201
- Snijders, L., Kewley, L. J., & van der Werf, P. P. 2007, *ApJ*, 669, 269
- Sobral, D., Best, P. N., Smail, I., et al. 2014, *MNRAS*, 437, 3516
- Speagle, J. S., Steinhardt, C. L., Capak, P. L., & Silverman, J. D. 2014, *ApJS*, 214, 15
- Spitzer, L. 1978, *Physical Processes in the Interstellar Medium* (New York: Wiley)
- Steidel, C. C., Erb, D. K., Shapley, A. E., et al. 2010, *ApJ*, 717, 289
- Steidel, C. C., Rudie, G. C., Strom, A. L., et al. 2014, *ApJ*, 795, 165
- Steidel, C. C., Strom, A. L., Pettini, M., et al. 2016, *ApJ*, 826, 159
- Stott, J. P., Swinbank, A. M., Johnson, H. L., et al. 2016, *MNRAS*, 457, 1888
- Strom, A. L., Steidel, C. C., Rudie, G. C., et al. 2017, *ApJ*, 836, 164
- Strom, A. L., Steidel, C. C., Rudie, G. C., Trainor, R. F., & Pettini, M. 2018, *ApJ*, 868, 117
- Sun, J., Leroy, A. K., Ostriker, E. C., et al. 2020, *ApJ*, 892, 148
- Swinbank, A. M., Harrison, C. M., Tiley, A. L., et al. 2019, *MNRAS*, 487, 381
- Tacchella, S., Carollo, C. M., Renzini, A., et al. 2015, *Sci*, 348, 314
- Tacconi, L. J., Genzel, R., Saintonge, A., et al. 2018, *ApJ*, 853, 179
- Tacconi, L. J., Genzel, R., & Sternberg, A. 2020, *ARA&A*, 58, 157
- Thilker, D. A., Waltherbos, R. A. M., Braun, R., & Hoopes, C. G. 2002, *AJ*, 124, 3118
- Übler, H., Genzel, R., Wisnioski, E., et al. 2019, *ApJ*, 880, 48
- van der Kruit, P. C. 1988, *A&A*, 192, 117
- van der Wel, A., Bell, E. F., Häussler, B., et al. 2012, *ApJS*, 203, 24
- van der Wel, A., Franx, M., van Dokkum, P. G., et al. 2014, *ApJ*, 788, 28
- Vazdekis, A., Sánchez-Blázquez, P., Falcón-Barroso, J., et al. 2010, *MNRAS*, 404, 1639
- Wang, J., Koribalski, B. S., Serra, P., et al. 2016, *MNRAS*, 460, 2143
- Weaver, R., McCray, R., Castor, J., Shapiro, P., & Moore, R. 1977, *ApJ*, 218, 377
- Westmoquette, M. S., Dale, J. E., Ercolano, B., & Smith, L. J. 2013, *MNRAS*, 435, 30
- Westmoquette, M. S., Smith, L. J., & Gallagher, J. S., III 2011, *MNRAS*, 414, 3719
- Whitaker, K. E., Franx, M., Leja, J., et al. 2014, *ApJ*, 795, 104
- Wielen, R. 1977, *A&A*, 60, 263
- Wilman, D. J., Fossati, M., Mendel, J. T., et al. 2020, *ApJ*, 892, 1
- Wisnioski, E., Förster Schreiber, N. M., Fossati, M., et al. 2019, *ApJ*, 886, 124
- Wisnioski, E., Förster Schreiber, N. M., Wuyts, S., et al. 2015, *ApJ*, 799, 209
- Wisnioski, E., Glazebrook, K., Blake, C., et al. 2012, *MNRAS*, 422, 3339
- Wuyts, E., Rigby, J. R., Gladders, M. D., et al. 2012a, *ApJ*, 745, 86
- Wuyts, E., Rigby, J. R., Sharon, K., & Gladders, M. D. 2012b, *ApJ*, 755, 73
- Wuyts, S., Förster Schreiber, N. M., Genzel, R., et al. 2012c, *ApJ*, 753, 114
- Wuyts, S., Förster Schreiber, N. M., Lutz, D., et al. 2011, *ApJ*, 738, 106
- Wuyts, S., Förster Schreiber, N. M., Nelson, E. J., et al. 2013, *ApJ*, 779, 135
- Zaritsky, D., Kennicutt, R. C., Jr., & Huchra, J. P. 1994, *ApJ*, 420, 87
- Zhang, K., Yan, R., Bundy, K., et al. 2017, *MNRAS*, 466, 3217